

## Editorial Board

**Dr. Mohammad I. Malkawi**

Associate Professor, Department of Software Engineering

**Jordan**

**Dr. Kaveh Ostad-Ali-Askari**

Assistant Professor, Department of Civil Engineering, Isfahan (Khorasgan) Branch,

**Iran**

**Dr. Mohammed A. Akour**

Associate Professor in the Department of Software Engineering,

**Jordan**

**Dr. Mohammad mehdi hassani**

Faculty of Computer Engineering

**Iran**

**Prof. Ratnakaram Venkata Nadh (Ph.D)**

Professor & Head - Chemistry Department, Dy. Director - Admissions

**India**

**Dr. SIDDIKOV ILKHOMJON KHAKIMOVICH**

Head of the Department of "Power Supply Systems",

**Uzbekistan**

**Dr. S. DHANASEKARAN**

Associate Professor in the Department of Computer Science and Engineering,

**India**

**Younes El Kacimi, Ph. D.**

Science Faculty, Department of Chemistry Kénitra

**Morocco**

**Denis Chemezov**

Lecturer, Vladimir Industrial College, Vladimir

**Russia**

**RICHARD O. AFOLABI, Ph.D.**

Department of Petroleum Engineering,

**Nigeria**

Volume 2 ISSUE 2

March-April 2018

## **Analysis of three-dimensional natural convection and entropy generation in a water filled open trapezoidal enclosure**

Walid Aich

## **On Carbon Emission Credits Options Pricing**

Richard OnyinoSimwa

## **Hypergiant –conducting nanogranular compound materials, as IR-photon detectors for Boson current transport at room temperature with GA/cm<sup>2</sup> current carrying capability**

Hans W.P. Koops

## **A BBO-based algorithm for the non-convex economic/environmental dispatch**

Asseri Ali Amer.M, Marouani Ismail.T

# Analysis of three-dimensional natural convection and entropy generation in a water filled open trapezoidal enclosure

Walid Aich<sup>1, 2</sup>

<sup>1</sup>Mechanical Engineering Department, University of Hail, Hail, KSA

<sup>2</sup>Research Unit of Materials, Energy and Renewable Energies (MEER), Tunisia

## ABSTRACT

A three-dimensional numerical analysis of laminar natural convection with entropy generation in an open trapezoidal cavity filled with water has been carried out. In this investigation, the inclined wall is maintained at isothermal hot temperature while cold water enters into the cavity from its right open boundary and all other walls are assumed to be perfect thermal insulators. Attention is paid on the effects of buoyancy forces on the flow structure and temperature distribution inside the open enclosure. Rayleigh number is the main parameter which changes from  $10^3$  to  $10^5$  and Prandtl number is fixed at  $Pr = 6.2$ . Obtained results have been presented in the form of particles trajectories, iso-surfaces of temperature and those of entropy generated as well as the average Nusselt number. It has been found that the flow structure is sensitive to the value of Rayleigh number and that heat transfer increases with increasing this parameter.

**Keywords**—Natural convection; Entropy generation; Trapezoidal cavity; Rayleigh number; Nusselt number

## I. INTRODUCTION

The analysis of natural convection in both enclosed and open cavities has received significant attention due to many engineering applications, such as, electronic equipment cooling, heat loss from solar collectors, food processing and storage, building insulation, fire control, metallurgy and flow in nuclear reactors. In recent decades, there have been numerous studies on natural convection due to thermal buoyancy effects inside trapezoidal cavities. Ilycan et al. [1,2] studied the natural convection motion and the heat transfer within a trapezoidal enclosure with parallel cylindrical top and bottom walls at different temperatures and plane adiabatic sidewalls. They presented both analytical and experimental results. Lam et al. [3] obtained similar results for a trapezoidal cavity having two vertical adiabatic walls, an inclined cold top wall and a hot floor. The effect of inclination angle of isothermal walls on flow structure for laminar natural convection flow in trapezoidal cavities was studied by Kuyper and Hoogendoorn [4]. They also analyzed the influence of Ra number on the average Nusselt number. Numerical investigation on natural convection within a partially divided trapezoidal cavity was carried out by Moukalled and Darwish [5]. Two different thermal boundary conditions were considered, case 1: the hot left wall and cold right wall and case 2: the hot right wall and cold left wall. It was found that the presence of the baffle decreases the overall heat transfer rate in the trapezoidal cavity, irrespective of the position and height of the baffle. They also observed that the maximum decrease in the heat transfer rate occurs for the baffle placed near to the left wall, irrespective of the baffle height. Moukalled and Darwish [6] further extended their study to investigate the effects of the height and position of the baffle protruding out from the inclined top wall, on the fluid flow and heat transfer in a trapezoidal enclosure with the similar thermal boundary conditions as mentioned in the earlier work [5]. Similarly, it was found that the overall heat transfer rate in the trapezoidal cavity is greatly reduced in the presence of the baffle, irrespective of the size and position of the baffle. The effect of the divider on natural convection in a partially divided trapezoidal enclosure under summer and winter boundary conditions was investigated by Arici and Sahin [7]. It was observed that there was no significant influence of the divider on the temperature distribution and consequently on the heat transfer rates during the summer boundary conditions. However, the heat transfer rate is reduced due to the presence of the divider during the winter boundary conditions. Silva et al. [8] analyzed the effect of the inclination angle of the top wall on the heat transfer rate in a trapezoidal cavity with two baffles placed on the cavity's horizontal surface. It was found that, the temperature and velocity gradients within the enclosure decrease with the height of the baffles. They also concluded that for a fixed height of baffles, the overall heat transfer rate increases with the inclination angle. Two-dimensional trapezoidal cavities find big place in literature [9–19]. However, to the best of the authors' knowledge, no attention has been paid to investigate natural convection and entropy generation in partially or wholly open three-

dimensional trapezoidal shaped spaces. Therefore, the main objective of the present study is to investigate numerically the laminar natural convection with entropy generation in an open three-dimensional trapezoidal cavity filled with water.

## II. MATHEMATICAL FORMULATION

### A. Physical model

Physical model is presented in fig. 1 with its specified coordinate system and boundary conditions. Indeed, the considered problem is three-dimensional natural convection and entropy generation in a one side opened trapezoidal cavity filled with water. The analyzed cavity is heated from inclined left wall and cooled from right open side while remaining walls are assumed to be insulated. The height, the length of the upper horizontal wall and the width of the cavity are equal to  $L$  while the length of the bottom wall is  $2L$ .

### B. Governing Equations and Numerical Solution

As numerical method we had recourse to the vorticity-potential vector formalism which allows, in a three-dimensional configuration, the elimination of the pressure, which is a delicate term to treat. To eliminate this term one applies the rotational to the equation of momentum. More details on this 3-D formalism can be found in the work of Kolsi et al. [20]. The potential vector and the vorticity are respectively defined by the two following relations:

$$\vec{\omega}' = \vec{\nabla} \times \vec{V}' \quad \text{and} \quad \vec{V}' = \vec{\nabla} \times \vec{\psi}' \quad (1)$$

$$-\vec{\omega} = \nabla^2 \vec{\psi} \quad (2)$$

$$\frac{\partial \vec{\omega}}{\partial t} + (\vec{V} \cdot \nabla) \vec{\omega} - (\vec{\omega} \cdot \nabla) \vec{V} = \Delta \vec{\omega} + Ra \cdot Pr \cdot \left[ \frac{\partial T}{\partial z}; 0; -\frac{\partial T}{\partial x} \right] \quad (3)$$

$$\frac{\partial T}{\partial t} + \vec{V} \cdot \nabla T = \Delta T \quad (4)$$

With:  $Pr = \frac{\nu}{\alpha}$  and  $Ra = \frac{g \cdot \beta \cdot \Delta T \cdot L^3}{\nu \cdot \alpha}$

Boundary conditions for considered model are given as follows:

#### Temperature:

$T = 1$  on the left inclined wall and  $T = 0$  on the right open side.

$\frac{\partial T}{\partial n} = 0$  on all other walls (adiabatic).

$T_{in} = 0$  if  $n \cdot V < 0$  at open boundary

$\left. \frac{\partial T}{\partial n} \right|_{out} = 0$  if  $n \cdot V \geq 0$  at open boundary

#### Velocity:

$V_x = V_y = V_z = 0$  on all walls

$\frac{\partial V_x}{\partial x} = \frac{\partial V_y}{\partial x} = \frac{\partial V_z}{\partial x} = 0$  at open boundary

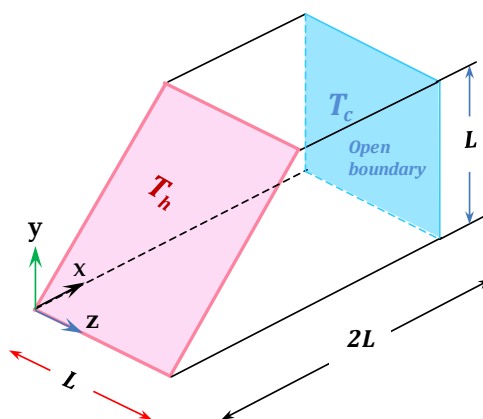


Fig. 1. Schematic of a water-filled open trapezoidal enclosure.

The generated entropy is written in the following form as:

$$S'_{gen} = -\frac{1}{T'^2} \cdot \vec{q} \cdot \vec{\nabla} T' + \frac{\mu}{T'} \cdot \phi'$$

The first term represents the generated entropy due to temperature gradient and the second that due to the friction effects.

$$\vec{q} = -k \cdot \text{grad} T'$$

The dissipation function is written in incompressible flow as:

$$\phi' = 2 \left[ \left( \frac{\partial V'_x}{\partial x'} \right)^2 + \left( \frac{\partial V'_y}{\partial y'} \right)^2 + \left( \frac{\partial V'_z}{\partial z'} \right)^2 \right] + \left( \frac{\partial V'_y}{\partial x'} + \frac{\partial V'_x}{\partial y'} \right)^2 + \left( \frac{\partial V'_z}{\partial y'} + \frac{\partial V'_y}{\partial z'} \right)^2 + \left( \frac{\partial V'_x}{\partial z'} + \frac{\partial V'_z}{\partial x'} \right)^2 \quad (5)$$

From where the generated entropy is written:

$$S'_{gen} = \frac{k}{T'^2_0} \left[ \left( \frac{\partial T'}{\partial x'} \right)^2 + \left( \frac{\partial T'}{\partial y'} \right)^2 + \left( \frac{\partial T'}{\partial z'} \right)^2 \right] + 2 \frac{\mu}{T'_0} \left\{ \left[ \left( \frac{\partial V'_x}{\partial x'} \right)^2 + \left( \frac{\partial V'_y}{\partial y'} \right)^2 + \left( \frac{\partial V'_z}{\partial z'} \right)^2 \right] + \left[ \left( \frac{\partial V'_y}{\partial x'} + \frac{\partial V'_x}{\partial y'} \right)^2 + \left( \frac{\partial V'_z}{\partial y'} + \frac{\partial V'_y}{\partial z'} \right)^2 + \left( \frac{\partial V'_x}{\partial z'} + \frac{\partial V'_z}{\partial x'} \right)^2 \right] \right\} \quad (6)$$

After adimensionalisation one obtains generated entropy number (dimensionless local entropy generated) which is written in the following way:

$$N_s = S'_{gen} \frac{1}{k} \left( \frac{L T_0}{\Delta T} \right)^2 \quad (7)$$

From where:

$$N_s = \left[ \left( \frac{\partial T}{\partial x} \right)^2 + \left( \frac{\partial T}{\partial y} \right)^2 + \left( \frac{\partial T}{\partial z} \right)^2 \right] + \varphi \cdot \left\{ 2 \left[ \left( \frac{\partial V_x}{\partial x} \right)^2 + \left( \frac{\partial V_y}{\partial y} \right)^2 + \left( \frac{\partial V_z}{\partial z} \right)^2 \right] + \left[ \left( \frac{\partial V_y}{\partial x} + \frac{\partial V_x}{\partial y} \right)^2 + \left( \frac{\partial V_z}{\partial y} + \frac{\partial V_y}{\partial z} \right)^2 \right] + \left[ \left( \frac{\partial V_x}{\partial z} + \frac{\partial V_z}{\partial x} \right)^2 \right] \right\} \quad (8)$$

With  $\varphi = \frac{\mu \alpha^2 T_m}{L^2 k \Delta T^2}$  is the irreversibility coefficient.

The first term of  $N_s$  represents the local irreversibility due to the temperatures gradients, it is noted  $N_{s-th}$ . The second term represents the contribution of the viscous effects in the irreversibility it is noted  $N_{s-fr}$ .  $N_s$  give a good idea on the profile and the distribution of the generated local dimensionless entropy. The total dimensionless generated entropy is written:

$$S_{tot} = \int_v N_s dv = \int_v (N_{s-th} + N_{s-fr}) dv = S_{th} + S_{fr} \quad (9)$$

The local and average Nusselt at the hot inclined wall are given by:

$$Nu = \frac{\partial T}{\partial n} \quad \text{and} \quad Num = \frac{\sqrt{2} L L}{\int_0^1 \int_0^1 Nu dn dz} \quad (10)$$

With:  $\vec{n}$  is the unit vector normal to the hot inclined wall.

It should be noted that numerical analysis has been developed using an in-house computational code on the basis of FORTRAN programming language. The time step ( $10^{-4}$ ) and spatial mesh ( $122 \times 61 \times 61$ ) are utilized to carry out all the numerical tests. The solution is considered acceptable when the following convergence criterion is satisfied for each step of time:

$$\sum_i^{1,2,3} \frac{\max |\psi_i^n - \psi_i^{n-1}|}{\max |\psi_i^n|} + \max |T_i^n - T_i^{n-1}| \leq 10^{-4} \quad (11)$$

### III. RESULTS AND DISCUSSION

Trajectories of particles and velocity magnitude for different Rayleigh number values are illustrated in fig. 2. It is noted that Prandtl number is fixed at  $Pr = 6.2$  for whole work and Rayleigh number is changed from  $10^3$  to  $10^5$ . The numerical result shows an incoming water flow at the lower part of the right open side while the internal hotter water is pushed outwards through its upper part. Therefore, as seen from the figure, particles circulate in clockwise direction by absorbing heat from the heated side

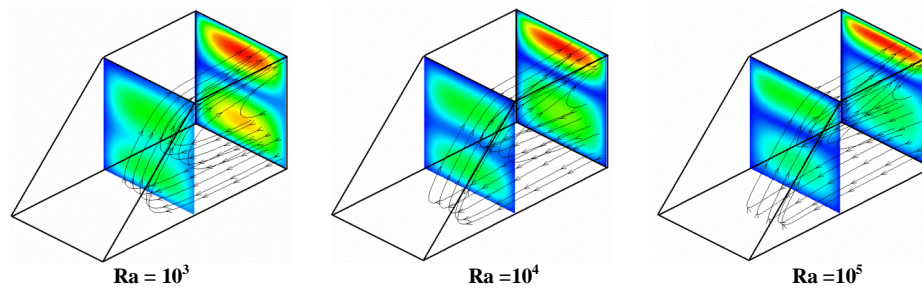


Fig. 2. Particles trajectory and velocity magnitude for different Rayleigh number values.

before leaving the cavity giving way to the cold particles to fill the cavity maintaining the cooling process. Thus a stream of water is produced with a front approaching the hot wall as the number of Rayleigh increases. Indeed, it can be noticed that the dead zone is reduced due to increasing of effectiveness of convection heat transfer. By increasing  $Ra$ , the heated and rising fluid leads to formation of the thermal boundary layer parallel to the inclined walls and there is a strong convective current resulting in a noticeable increase in the velocity magnitude at the upper part of the open side of the cavity while the left lower corner remains as stagnant zone. The highest magnitude of velocity occurred for  $Ra = 10^5$ .

Fig. 3 depicts the iso-surfaces of temperature for different Rayleigh number values. When the conduction is the dominant mode of heat transfer ( $Ra = 10^3$ ), the isotherms present an almost vertical stratification and water is nearly at rest. It is obvious that these iso-surfaces are always orthogonal the adiabatic walls. By increasing Rayleigh number ( $Ra \geq 10^4$ ), heated water near the hot wall is increasingly driven by the incoming water flow at the lower part of the cavity making inclined stratification near the heated side and horizontal stratification near the upper horizontal wall. Thus an excessive temperature gradient near the lower part of the hot wall took place. It should be noted that the entering water is cold and such penetration of low temperature wave leads to a formation of thin thermal boundary layer near the inclined hot wall. The latter characterizes a heating of the cavity upper part due to an appearance of ascending flow along the hot wall where cold water is heated. The mentioned thin thermal boundary layer illustrates the intensive motion of the water near the inclined wall.

It is noticed that the rate of heat transfer inside the enclosure is measured in term of the overall Nusselt number. Therefore, fig. 4 shows the variation of the average Nusselt number, which characterizes the heat transfer from the hot wall towards the vicinity of the enclosure, with the Rayleigh number. It is obvious that for low values of  $Ra$  and when the conduction is the dominant mode of heat transfer, this variation is insignificant. However, for heat removal from the heated inclined wall increases by means of increasing Rayleigh number and the maximum rate is obtained for the highest  $Ra$  as expected. Indeed, by increasing Rayleigh number to  $10^5$ , the fluid flow intensifies and the thermal energy transport from the hot wall increases due to the enhancement of convection heat transfer.

To achieve a maximum heat transfer rate between the heated side and the cooling water, it is essential to carry out an entropy generation analysis to investigate the two sources of irreversibilities that are responsible for heat losses. These irreversibilities are mainly due to heat transfer and fluid friction.

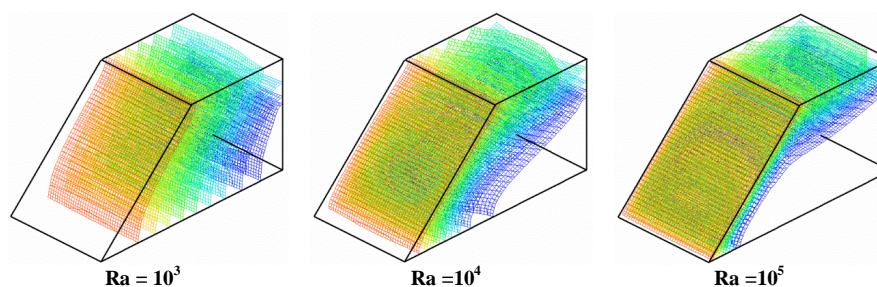


Fig. 3. Iso-surfaces of temperature for different Rayleigh number values.

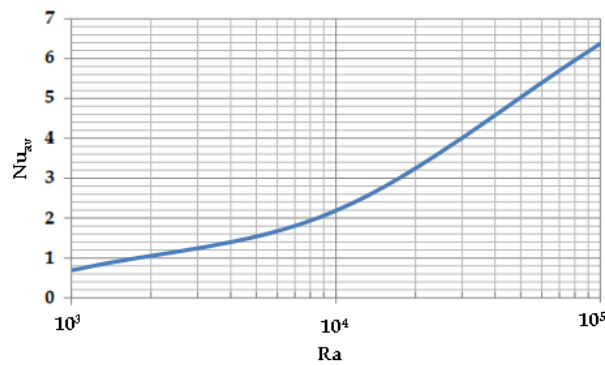


Fig. 4. Variation of Mean Nusselt number on hot wall with Rayleigh number.

Therefore, iso-surfaces of entropy generation (entropy generation due to heat transfer, entropy generation due to fluid friction and the total entropy generation) are shown in fig. 5 for an irreversibility coefficient and different values of Rayleigh number. It can be noticed that, for the lowest value of Rayleigh number ( $Ra = 10^3$ ), the generated entropy covers the entire trapezoidal enclosure. However, for , the generated entropy concentrates (locates itself) along the inclined and upper horizontal walls. This result supports our observations made during the discussion on the particles trajectory and temperature distribution and can explain the boundary layer phenomenon met for the great Rayleigh number values. The maximum of entropy generation due to heat transfer  $S_{th}$  is located in the region near the center of the inclined hot wall. Moreover, it can be observed that the entropy generation due to heat transfer and total entropy generation follow nearly the same distribution which gives a clue that entropy due to heat transfer outweighs that due to fluid friction.

Such a result is supported by fig. 6 showing the entropy generation due to heat transfer, the entropy generation due to friction and the total entropy generation as function of Rayleigh number. In fact, irrespective the value of  $Ra$ , entropy generation due to viscous irreversibility is less significant in deciding the total entropy generation, which is sum of entropy generations due to heat transfer and friction.

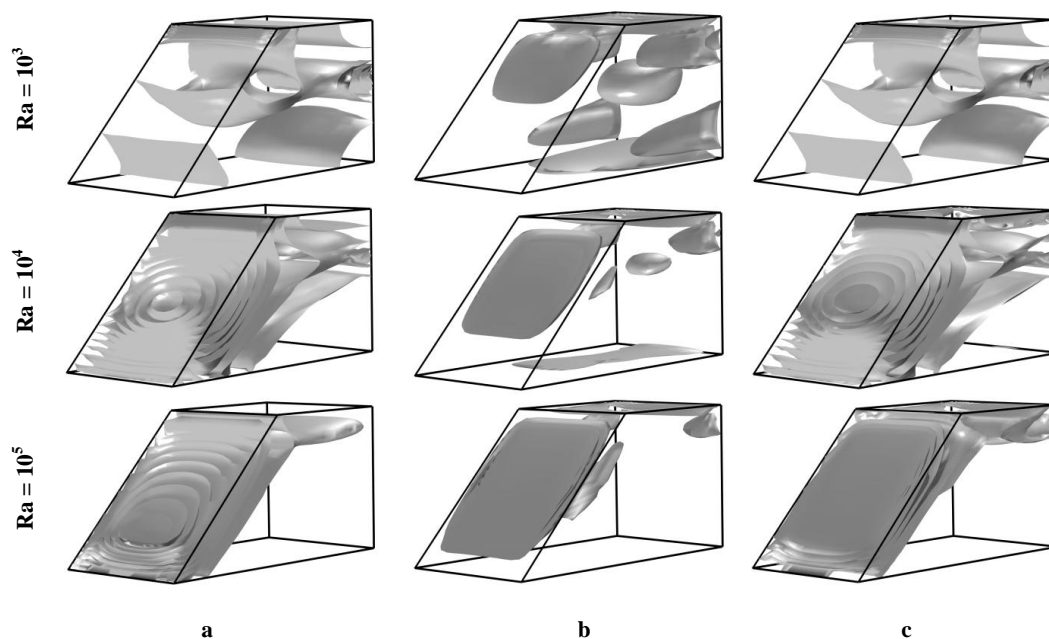


Fig. 5. Iso-surfaces of entropy generation a) Entropy generation due to heat transfer, b) Entropy generation due to fluid friction, c) Total entropy generation for  $\varphi = 10^{-5}$

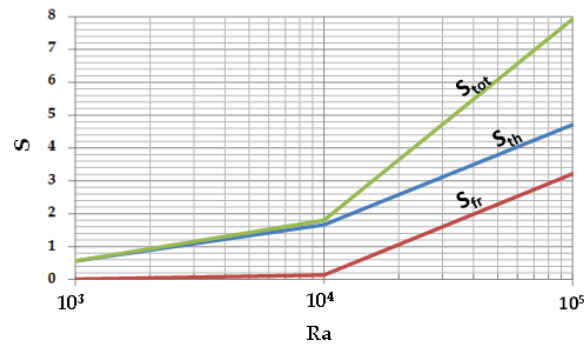


Fig. 6. Variation of entropy generation with Rayleigh number

#### IV. CONCLUSIONS

Three-dimensional numerical investigation has been carried out to simulate natural convection and entropy generation in a water filled open trapezoidal enclosure. Results are presented for different Rayleigh number values which is the main parameter of the study. Some conclusions can be drawn as follows:

- For lower values of Rayleigh number, conduction is the primary mode of heat transfer and the flow strength is very low due to poor convective heat transfer.
- Flow strength increases with increasing of Rayleigh number and a strong convective current is noticeable along the hot wall where cold water is heated.
- The increasing of Ra leads to a formation of thin thermal boundary layer near the inclined hot wall resulting in a heating of the cavity upper part due to an appearance of ascending flow along the hot wall where cold water is heated.
- The flow structure and the magnitude of velocity are sensitive to the value of Rayleigh number.
- Overall Nusselt number at the heated surface increases with increasing value of Ra indicating a maximum heat transfer rate at  $Ra=10^5$ .
- Irreversibilities are mainly due to heat transfer especially at low Rayleigh number values.

#### REFERENCES

- [1] L. Iyican, Y. Bayazitoglu, and L.C.Witte, "Analytical study of natural convective heat transfer within trapezoidal enclosure", J. Heat Transfer, Vol.102, No. 8, 1980, pp. 640-647.
- [2] L. Iyican, L.C. Witte, and Y. Bayazitoglu, "An experimental study of natural convection in trapezoidal enclosures", J. Heat Transfer, Vol.102, No. 8, 1980, pp. 648-653.
- [3] S.W.Lam, R. Gani, and J.G. Simons, "Experimental and numerical studies of natural convection in trapezoidal cavities", J. Heat Transfer, Vol.111, No. 2, 1989, pp. 372-377.
- [4] R.A. Kuypers, and C.J. Hoogendoorn, "Laminar natural convection flow in trapezoidal enclosures", Numer. Heat Transfer, Part A, Vol. 28, No. 1, 1995, pp. 55-67.
- [5] F. Moukalled, and M. Darwish, "Natural convection in a partitioned trapezoidal cavity heated from the side", Numer. Heat Transfer A, Vol. 43, No. 5, 2003, pp. 543-563.
- [6] F. Moukalled, and M. Darwish, "Natural convection in a trapezoidal enclosure heated from the side with a baffle mounted on its upper inclined surface", Heat Transfer Eng, Vol. 25, No. 8, 2004, pp. 80-93.
- [7] M.E. Arici, and B. Sahin, "Natural convection heat transfer in a partially divided trapezoidal enclosure", Therm. Sci, Vol.13, No. 4, 2009, pp. 213-220.
- [8] A. Silva, E. Fontana, V.C. Mariani, and F. Marcondes, "Numerical investigation of several physical and geometric parameters in the natural convection into trapezoidal cavities", Int. J. Heat Mass Transfer, Vol.13, No. 4, 2012, pp. 6808-6818.
- [9] T. Basak, S. Roy, and I. Pop, "Heat flow analysis for natural convection within trapezoidal enclosures based on heatline concept", Int. J. Heat Mass Transfer, Vol.11, No. 11-12, 2009, pp. 2471-2483.
- [10] K. Lasfer, M. Bouzaiane, and T. Lili, "Numerical study of laminar natural convection in a side-heated trapezoidal cavity at various inclined heated sidewalls", Heat Transfer Eng, Vol. 31, No. 5, 2010, pp. 362-373.

- [11] D. Ramakrishna, T. Basak, S. Roy, and E. Mamoniati, "Analysis of thermal efficiency via analysis of heat flow and entropy generation during natural convection within porous trapezoidal cavities", *Int. J. Heat Mass Transfer*, Vol. 77, 2014, pp. 98-113.
- [12] T. Basak, R. Anandalakshmi, S. Roy, and I. Pop, "Role of entropy generation on thermal management due to thermal convection in porous trapezoidal enclosures with isothermal and non-isothermal heating of wall", *Int. J. Heat Mass Transfer*, Vol. 67, 2013, pp. 810-828.
- [13] D. Ramakrishna, T. Basak, and S. Roy, "Heatlines for visualization of heat transport for natural convection within porous trapezoidal enclosures with various wall heating", *Numer. Heat Transfer A*, Vol. 63, 2012, pp. 347-372.
- [14] Y. Varol, "Natural convection for hot materials confined within two entrapped porous trapezoidal cavities", *Int. Commun. Heat Mass Transfer*, Vol. 39, No. 2, 2012, pp. 282-290.
- [15] T. Basak, S. Roy, A. Matta, and I. Pop, "Analysis of heatlines for natural convection within porous trapezoidal enclosures: effect of uniform and non-uniform heating of bottom wall", *Int. J. Heat Mass Transfer*, Vol. 53, 2010, pp. 5947-5961.
- [16] R. Roslan, H. Saleh, and I. Hashim, "Buoyancy-driven heat transfer in nanofluid filled trapezoidal enclosure with variable thermal conductivity and viscosity", *Numer. Heat Transfer A*, Vol.10, 2011, pp. 867-882.
- [17] H. Saleh, R. Roslan, and I. Hashim, "Natural convection heat transfer in a nanofluid filled trapezoidal enclosure", *Int. J. Heat Mass Transfer*, Vol. 54, No. 1-3, 2011, pp. 194-201.
- [18] B.V.R. Kumar, and B. Kumar, "Parallel computation of natural convection in trapezoidal porous enclosures", *Math. Comput. Simul*, Vol. 65, No. 3, 2004, pp. 221-229.
- [19] A.C. Baytas, and I. Pop, "Natural convection in a trapezoidal enclosure filled with a porous medium", *Int. J. Eng. Sci*, Vol. 39, No. 2, 2001, pp. 125-134.
- [20] L. Kolsi, A. Abidi, M.N. Borjini, N. Daous, and H. Ben Aïssia, "Effect of an external magnetic field on the 3-D unsteady natural convection in a cubical enclosure", *Numerical Heat Transfer Part A*, Vol. 51, No. 10, 2007, pp. 1003-1021.

# On Carbon Emission Credits Options Pricing

Richard OnyinoSimwa

Division of Actuarial Science & Financial Mathematics,

School of Mathematics, University of Nairobi

## ABSTRACT

The effect of adverse climate change is of major concern worldwide and several approaches are being developed to mitigate against anticipated economic and social disaster. Carbon emissions has been identified as a major contributor to the adverse climate change and following the Kyoto protocol, European countries have, through a caucus, effected a market to reward or fine members depending on their compliance position. The commodity for the market is the carbon emission credits. Stochastic models for pricing of options on these credits are considered in this paper. In particular, we determine the price basing on the Normal Inverse Gaussian and the Brownian Motion models. Maximum Likelihood Estimation is applied to determine model parameter estimates in each case. It is shown that the Normal Inverse Gaussian model has a better fit to the data but gives higher prices for a given strike price, compared to the Brownian Motion model.

**Key Words:** Carbon Emission Credit, Brownian Motion, Kyoto Protocol Compliance, Normal Inverse Gaussian Distribution, Fourier Transform, Risk-Neutral Option Pricing.

## I. INTRODUCTION

Greenhouse gas (GHG) emissions come from the burning of fossil fuels for energy (e.g. for electricity and transport). When oil, gas or coal burns, carbon contained within it combines with oxygen in the air to create carbon dioxide. Globally, almost 80% of GHG emissions come from human sources. Global GHG emissions grew by approximately 42% between 1990 and 2011, with the bulk growth occurring in emerging markets and developing countries.

The release of GHGs and their increasing concentration in the atmosphere are already having an impact on the environment, human health and the economy. These impacts are expected to become more severe, unless concerted efforts to reduce emissions are undertaken. Environmental impacts include the following. Annual temperatures are expected to rise, increased coastal flooding due to increased temperatures, heat waves that could result to forest fires and Shrinking water supplies. Human health impacts include high temperatures that may increase the risk of deaths from dehydration and heat stroke, an increase in water-, food-, vector- and rodent-borne diseases, cancer diseases that develop due to air pollution. Economic impacts include agriculture, forestry, tourism and recreation being affected by changing weather patterns and damage to infrastructure caused by extreme weather events.

In order to address climate change globally, the Kyoto Protocol was introduced. The Kyoto Protocol is an international agreement linked to the United Nations Framework Convention on Climate Change, which commits its parties by setting international binding emission reduction targets.

The Kyoto Protocol was adopted in Kyoto, Japan, on 11 December 1997 and entered into force on 16th February, 2005. Participating countries that have ratified the Kyoto Protocol have committed to cut GHG emissions. The Kyoto Protocol sets binding emission reduction targets for participants. The goal of Kyoto was to see participants collectively reducing emissions of greenhouse gases by 5.2% below the emission levels of 1990 by 2012.

Binding emissions reduction commitment for participants meant that the space to pollute was limited, and what is scarce and essential commands a price. Greenhouse gas emissions- most prevalently carbon dioxide- became a new commodity. Kyoto Protocol now began to internalize what was now recognized as an unpriced externality. Since carbon dioxide is the principle greenhouse gas, people speak simply of trading in carbon.

This leads us to the second, the flexible mechanisms of the Kyoto Protocol, based on the trade of emissions permits. Kyoto Protocol countries bound to targets have to meet them largely through domestic action- that is, to reduce their emissions onshore. But they can meet part of their targets through the "market-based mechanisms" that ideally encourage GHG abatement to start where it is most cost-effective- for example, in the developing world. Quite simply, it does not matter where emissions are reduced, as long as they are removed from the planet's atmosphere. The Kyoto mechanisms are, International Emissions Trading (IET), Clean Development Mechanism (CDM) and Joint Implementation (JI).

Parties with commitments under the Kyoto Protocol that have accepted targets for limiting or reducing emissions are called Annex I parties. These countries are set a legally binding cut for GHG emission to 5.2% below their 1990 level. This reduction is to be attained in sum over all Annex I members over a five year compliance period which is from 2008 to 2012. The concrete implementation is as follows: Each Annex I member is assigned a certain Carbon dioxide gas amount, which equals to  $(5 \text{ years}) \times (\text{country's emission in 1990}) \times (1 - 0.0052)$ . This credit is measured in the so- called Assigned Amount Units (AAUs), corresponding to one ton of carbon dioxide. Each member faces penalties if its entire emission within the compliance period 2008-2012 exceeds member's total number of AAUs.

The IET mechanism allows annex I members that have emission units to spare to sell the excess to annex I members that are over their targets. Therefore, the carbon allowances traded in IET mechanism are called AAUs.

The CDM mechanism allows an Annex I member to implement an emission-reduction project in developing countries. Such projects can earn saleable certified emission reduction (CER) credits, each equivalent to one tonne of Carbon dioxide gas, which can be counted towards meeting Kyoto targets.

## II. LITERATURE REVIEW

Carmona and Hinz(2011) examined the spot EUA returns that exhibit a volatility clustering feature and the carbon market system that is impacted by the announcements of CO<sub>2</sub> emissions policies. They proposed a regime-switching jump diffusion model (RSJM) with a hidden Markov chain to capture not only a volatility clustering feature, but also the dynamics of the spot EUA returns that are influenced by change in the CO<sub>2</sub> emissions policies, and thereby altering jump arrivals. They concluded that RSJM is the best model to fit the price behavior of the carbon markets and to price its related derivatives.

Chevallier, J. and Sevi B. (2014) argue that jumps need to be explicitly taken into account when modeling spot and future carbon price series. He says that there is evidence that suggests that carbon futures are a pure jump process without a continuous component and a relatively high activity index. The occurrence of jumps on the carbon market may be related to information disclosure about allocation, or changes in the perimeter of the scheme. He concludes that derivatives models such as the models by Cont and Tankov (2004), and the CGMY model (Carr et al. (2002)) would be plausible candidates, since these models accommodate a pure-jump stochastic process with activity indices above unity, as found in the carbon futures data.

Seifert et al(2007) explain that European call and put options are actively traded on EUA future contracts. Since 2006, trades of options maturing in December of each year (prior to 2012) have produced a term structure of option prices. It is noted that, whether or not traders are using Black-Scholes to price options on EUAs and future contracts, it is important to have option price formulas based on underlying martingale with binary terminal value.

Bolviken and Benth(2000) argued that traders of carbon emissions need to have a valid carbon dioxide spot price model so that it can be possible to value potential derivatives and so that carbon emitting companies can be able to better assess their production costs and support emissions-related investment decisions. They therefore presented a tractable stochastic equilibrium model reflecting stylized features of the emissions trading scheme and analyzed the resulting carbon spot price dynamics. Their main findings were that carbon prices do not have to follow any seasonal patterns, discounted prices and should possess the martingale property, and an adequate carbon price process should exhibit a time- and price- dependant volatility structure.

Carmona and Hinz (2011) argue that martingales finishing at two-valued random variables can be considered as basic building blocks which form the risk-neutral futures price dynamics. They therefore suggest a model for two-valued martingales, flexible in terms of time- and space changing volatility and capable to match the observed historical or implied volatility of the underlying future.

However, Bolviksen and Benth (2000), argue that the family of Normal Inverse Gaussian (NIG) distribution is able to portray stochastic phenomena that have heavy tails or are strongly skewed. In addition to that, NIG distributions are not confined to the positive half axis. Therefore, with the NIG distribution the financial analyst has at its disposal a model that can be adapted to many different shapes while the distribution of sums of independent random variables are still trivial to compute.

### III. METHODOLOGY

#### 3.1.1 Levy Process

**Definition 1.1** A cadlag real valued stochastic process  $\{X(t)\}_{t \geq 0}$  such that  $X(0) = 0$  is called a Levy Process if it has stationary independent increments and is stochastically continuous.

#### **Brownian motion**

The *Brownian motion* is a Levy process that has a drift. The standard Brownian motion follows a normal distribution with mean  $\mu$  and variance  $\sigma^2$ .

#### 3.1.2 Normal Inverse Gaussian process (NIG)

The *Normal inverse Gaussian process* (NIG) is a Levy process  $\{X(t)\}_{t \geq 0}$  that has normal inverse Gaussian distributed increments. Specifically,  $X(t)$  has a  $NIG(\alpha, \beta, \delta t, \mu t)$  – distribution with parameters  $\alpha > 0, |\beta| < \alpha, \delta > 0$  and  $\mu \in \mathbb{R}$ .

The  $NIG(\alpha, \beta, \delta, \mu)$  – distribution has a probability density function

$$f_{NIG(x;\alpha,\beta,\delta,\mu)} = \frac{\alpha\delta}{\pi} \frac{K_1(\alpha\sqrt{\delta^2 - (x-\mu)^2})}{\sqrt{\delta^2 + (x-\mu)^2}} \exp\{\delta\sqrt{\alpha^2 - \beta^2 + \beta(x-\mu)}\}$$

Where

$$K_n(Z) = \frac{1}{2} \int_0^\infty u^{n-1} \exp\{-\frac{Z}{2}(u + \frac{1}{u})\} du$$

is the modified Bessel function of the third kind, while the characteristic function is given by

$$\phi_{NIG}(u) = \exp(-\delta(\sqrt{\alpha^2 - (\beta + iu)^2} - \sqrt{\alpha^2 - \beta^2}))e^{i\mu u}.$$

The mean, variance, skewness and kurtosis of NIG distribution are

$$\text{Mean} = \mu + \frac{\beta\delta}{\sqrt{\alpha^2 - \beta^2}}$$

$$\text{Variance} = \frac{\delta\alpha^2}{(\sqrt{\alpha^2 - \beta^2})^3}$$

$$\text{Skewness} = \frac{3\beta}{\alpha(\delta\sqrt{\alpha^2 - \beta^2})^{\frac{1}{2}}}$$

$$\text{Kurtosis} = 3 \left( 1 + \frac{\alpha^2 + 4\beta^2}{\delta\alpha^2\sqrt{\alpha^2 - \beta^2}} \right)$$

### 3.1.3 Symmetric Normal Inverse Gaussian distribution

The Symmetric NIG Levy process has symmetric NIG marginals. The NIG distribution is symmetric when the skewness parameter  $\beta = 0$ . In this case, the density of a symmetric NIG is

$$f_{NIG}(x) = \frac{\alpha}{\pi} e^{\alpha\delta} \frac{K_1 \left( \alpha\delta \sqrt{1 + \left( \frac{x-\mu}{\delta} \right)^2} \right)}{\sqrt{1 + \left( \frac{x-\mu}{\delta} \right)^2}}$$

It follows from the equations of the mean, variance and kurtosis, that  $\mu$  is mean,  $\frac{\delta}{\alpha}$  is variance and  $3 + \frac{3}{\alpha\delta}$  is kurtosis. We will denote the distribution of symmetric NIG by  $SNIG(\alpha, 0, \delta, \mu)$

The characteristic function for symmetric NIG is

$$\phi(u) = e^{iu\mu} e^{\alpha\delta \left( 1 - \sqrt{1 + \left( \frac{u}{\alpha} \right)^2} \right)} \tag{i}$$

By an inspection of the characteristic function we can see that the characteristic generator of symmetric Normal inverse Gaussian distribution is given by

$$\psi(v) = e^{\zeta \left( 1 - \sqrt{1 + \frac{2v}{\zeta}} \right)} \tag{ii}$$

where,  $\zeta = \alpha\delta$

### 3.2 BASIC MODELLING OF THE COMPLIANCE EVENT ( see Carmona and Hinz(2011) )

In the one-period setting, credits are allocated at the beginning of the period to enable allowance trading until time  $T$  and to encourage agents to exercise efficient abatement strategies. At the compliance date  $T$ , market participants cover their emissions by redeeming allowances or pay a penalty  $\pi$  per unit of pollution not offset by credits. In this one-period model, unused allowances expire and are worthless because we do not allow for banking into the next period. At compliance date  $T$  the allowance price  $S_T$  is a random variable taking only the values 0 and  $\pi$ . More precisely, if the market remains under the target pollution level, then the price approaches zero. Otherwise, the allowance price tends to the penalty level  $\pi$ .

All the relevant asset price evolutions are assumed to be given by adapted stochastic processes on a filtered probability space  $(\Omega, F, P, (F_t)_{t \in [0, T]})$  on which we fix an equivalent probability measure  $Q \sim P$  which we call the spot martingale measure.

We denote by  $(S_t)_{t \in [0, T]}$  the price process of a future contract with maturity date  $T$  written on the allowance price. Given the digital nature of the terminal allowance price,  $S_T$  the central object of our study is the event  $N \subset F_T$  of non-compliance which settles the  $\{0, \pi\}$ -dichotomy of the terminal future prices by  $S_T = \pi 1_N$ .

Furthermore, a standard no-arbitrage argument shows that the future prices  $(S_t)_{t \in [0, T]}$  needs to be a martingale for the spot martingale measure,  $\mathbb{Q}$ . Hence, the problem of allowance price modeling reduces to the appropriate choice of the martingale

$$A_t = \pi E^{\mathbb{Q}}(1_N | F_t), t \in [0, T]$$

We choose our starting point to be the non-compliance event  $N \in F_T$  which we describe as the event where a hypothetic positive-valued random variable  $\Gamma_T$  exceeds the boundary 1, say  $N = \{\Gamma_T \geq 1\}$ . If one denotes by  $E_T$  the total pollution within the period  $[0, T]$  which must be balanced against the total number  $\gamma \in (0, \infty)$  of credits issued by the regulator, then the event of non-compliance should be given by  $N = \{E_T \geq \gamma\}$  which suggests that  $\Gamma_T$  should be viewed as the normalized total emission  $E_T / \gamma$ . However in our modeling, we merely describe the non-compliance event. Strictly speaking, so any random variable  $\Gamma_T$  with

$$\{\Gamma_T \geq 1\} = \{E_T / \gamma \geq 1\},$$

would do as well. On this account, we do not claim that  $\Gamma_T$  represents the total normalized emission  $E_T / \gamma$ . So the allowance Spot price is given by the martingale

$$A_t = \pi E^{\mathbb{Q}}(1_{\{\Gamma_T \geq 1\}} | F_t), t \in [0, T] \tag{1}$$

where  $A_t = S_t$  in this case. simplifying the notation, we consider the normalized futures price process

$$a_t := \frac{S_t}{\pi} = E^{\mathbb{Q}}(1_{\{\Gamma_T \geq 1\}} | F_t), t \in [0, T]$$

The random variable  $\Gamma_T$  is chosen from a suitable parameterized family of random variables.

The random variable  $\Gamma_T$  modeled by geometric Brownian motion (gbm) is given by

$$\Gamma_T = \Gamma_0 e^{\int_0^T \sigma_s dW_s - \frac{1}{2} \int_0^T \sigma_s^2 ds},$$

where  $W_t$  is a standard Brownian motion and  $\sigma$  is the volatility parameter. Since  $\mu_{gbm} = 0$ ,  $\Gamma_T$  is a martingale with respect to the underlying Brownian motion. which is given by,

$$a_t = \Phi \left( \frac{\Phi^{-1}(a_0) \sqrt{\int_0^T \sigma_s^2 ds} + \int_0^t \sigma_s dW_s}{\sqrt{\int_t^T \sigma_s^2 ds}} \right) \tag{2}$$

and it solves the stochastic differential equation

$$dS_t = \pi \Phi'(\Phi^{-1}(S_t)) \sqrt{Z_t} dW_t \tag{3}$$

where the positive valued function  $(0, T) \ni t \rightarrow Z_t$  is given by

$$Z_t = \frac{\sigma_t^2}{\int_t^T \sigma_u^2 du}, t \in [0, T] \tag{4}$$

The martingale is a random variable taking only the values 0 and  $\pi$  and satisfies

$$P\{\lim_{t \rightarrow T} a_t \in \{0, 1\}\} = 1 \tag{6}$$

As an alternative model for  $\Gamma_T$  we introduce the geometric Levy process

$$\Gamma_T = \Gamma_0 \exp(\mu_{nig}(t) + Y_t)$$

where  $Y_t$  is a normal inverse Gaussian Levy process and  $Y_T = \sum_{t=1}^T \Delta Y_t$ , where  $t = 1, \dots, N$  are i.i.d.

If we specify the parameters at time  $t=1$ , the first two moments (expectation and variance) are

$$E[Y_1] = \frac{\delta\beta}{\sqrt{\alpha^2 - \beta^2}}, \quad Var[Y_1] = \frac{\delta\alpha^2}{(\alpha^2 - \beta^2)^{3/2}}$$

This means that the log returns with time increment equal to 1 have expectation  $\mu_{nig} + E[Y_1]$  (or volatility)

$Var[Y_1]$  when they are modeled as independent normally inverse Gaussian distributed variables. We should note that when using the NIG process for option pricing, the location parameter of the distribution has no effect on the option value, so for convenience we will take  $\mu_{nig} = 0$

Since we have an infinitely divisible characteristic function, we can define the NIG process  $Y_t = \{Y_t, t \geq 0\}$ , which starts at zero and has independent and stationary increments each with a  $NIG(\alpha, \beta, \delta)$  distribution and the entire process has a  $NIG(\alpha, \beta, \delta t)$  law.

**Note:**  $Y_t = Y_{(T(t))}$  for each  $t \geq 0$ , where  $T(t)$  is an inverse Gaussian subordinator,  $IG(l; a, b)$ , which is independent of the standard Brownian motion with parameters  $a = 1$  and  $b = \delta\sqrt{\alpha^2 - \beta^2}$

We have the following connection between the parameters in the geometric Brownian motion and normal inverse Gaussian models

$$\mu_{gbm} = \mu_{nig} + \frac{\delta\beta}{\sqrt{\alpha^2 - \beta^2}}, \quad \sigma^2 = \frac{\delta\alpha^2}{(\alpha^2 - \beta^2)^{3/2}}.$$

The Levy-Kintchine representation of  $Y_t$  is

$$Y_t = \xi t + \int_0^t \int_{\mathbb{R} \setminus \{0\}} z \tilde{N}(dt, dz), \quad \xi = E[Y_1],$$

where  $N(dt, dz)$  is a Poisson random measure and  $\tilde{N}(dt, dz) = N(dt, dz) - dt \times n(dz)$  is the compensated Poisson random measure associated to  $Y_t$ . The Levy measure of  $Y_t$  is

$$n(dz) = \frac{\delta\alpha}{\pi |z|} \exp(\beta z) K_1(\alpha |z|) dz.$$

It follows from the Levy-Khintchine representation that the normal inverse Gaussian Levy process is a pure jump process.

In the symmetric case (i.e., when  $\beta = 0$ ), we have  $\mu_{gbm} = \mu_{nig}$  and  $\sigma^2 = \frac{\delta}{\alpha}$ .  $Y_t$  is a martingale with respect to its own filtration when  $E[Y_1] = \xi = 0$ , which is equivalent to  $\beta = 0$ .

Therefore

$$\Gamma_t = \Gamma_0 \exp(Y_t) \tag{5}$$

$$\begin{aligned} a_t &= E^Q \left( \mathbf{1}_{\{\Gamma_T \geq 1\}} \mid F_t \right) = Q \{ \Gamma_T \geq 1 \mid F_t \} \\ &= Q \{ \Gamma_0 e^{Y_t} \geq 1 \mid F_t \} \end{aligned} \tag{6}$$

The characteristic triplet of  $Y_t$  is  $(\mu, c, n(dz))$ , where  $c$  is used to define the Brownian component. In this case we will assume that  $c \neq 0$ .

We denote by  $S(\mu, \sigma^2, \psi)$  the distribution of  $Y_1$  whose characteristic function is of the form

$$\varphi_{Y_1}(u) = e^{i\mu u} \psi \left( \frac{\sigma^2}{2} u^2 \right), \tag{7}$$

The function  $\psi(u) : [0, \infty]$  is called the characteristic generator. It is unique up to scaling and if chosen such that  $\psi'(0) = -1$ , yields that  $\mu$  and  $\sigma^2$  are the mean and variance of  $Y_1$  respectively.

Under  $Q$ ,  $Y_t$  remains a symmetric NIG Levy process with characteristic triplet  $(\tilde{\mu}, \sigma^2, \psi)$ , where

$$\tilde{\mu}_1 = r - \ln(-\sigma^2 / 2)$$

$r$  is the risk free rate.

Now it is easy to see that  $Q_1$  is a natural equivalent martingale measure. Indeed, since  $-Y_t$  is a Levy process with P-characteristic triplets  $(-\mu, c, n(dz))$  and since the distribution of  $-Y_1$  is  $S(-\mu, \sigma^2, \psi)$ ,  $Q_1$  is chosen so that

$$\tilde{\mu}_1 = r + \ln(-\sigma^2 / 2)$$

By the uniqueness of  $(\tilde{\mu}_1)$ ,  $Q_1$  is unique.

Under  $Q_1$ ,  $Y_t$  is a symmetric NIG Levy process with marginal distribution from the family  $S(\tilde{\mu}t, \sigma t, \psi_t)$

**Proposition:** Denote by  $F_T$  the P-distribution function of the standardized variable  $(Y_T - \mu T) / (\sigma\sqrt{T})$ :

$$F_T(y) = P(Y_T \leq \sigma\sqrt{T}y + \mu T).$$

Then

$$F_T(y) = Q(Y_T \leq \sigma\sqrt{T}y + \tilde{\mu}T) = Q_1(Y_T \leq \sigma\sqrt{T}y + \tilde{\mu}_1T)$$

We will approximate the standardized symmetric NIG distribution by the standard normal.

$$\begin{aligned} a_t &= E^Q(1_{\{\Gamma_T \geq 1\}} | F_t) = Q\{\Gamma_T \geq 1 | F_t\} \\ &= \Phi\left(\frac{\ln \Gamma_0 + (r + \ln \psi(-\sigma^2/2))t}{\sigma\sqrt{t}}\right) \end{aligned} \tag{8}$$

By (ii) and  $\zeta = \alpha\delta = \alpha^2\sigma^2$ , we obtain

$$\ln \psi\left(-\frac{\sigma^2}{2}\right) = \zeta\left(1 - \sqrt{1 - \frac{\sigma^2}{\zeta}}\right) = \alpha^2\sigma^2 - \alpha\sigma^2\sqrt{\alpha^2 - 1}.$$

Equation (8) becomes

$$a_t = \Phi\left(\frac{\ln \Gamma_0 + (r + \alpha^2\sigma^2 - \alpha\sigma^2\sqrt{\alpha^2 - 1})t}{\sigma\sqrt{t}}\right), \tag{9}$$

**Remark:** If the excess emissions have a normal distribution (Normal inverse Gaussian) then the price process automatically becomes a normal distribution (Normal inverse Gaussian).

### 3.3 Estimation of Model Parameters

Parameter estimates that are such that the model lead to best fit to the carbon price data are determined. By using the NIG model, it means that we have four parameters that need to be estimated. While for the normal distribution, only two parameters need to be estimated. Given data we obtain these estimates for the parameters.

To obtain estimates of the parameters, maximum likelihood estimation method is applied. Thus the likelihood function is maximized with respect to the parameters. Hence, we seek the parameter values that maximizes the likelihood function

$$L(\theta) = \prod_{i=1}^n f(x_i; \theta)$$

We obtain the MLE estimate by maximizing the log likelihood function. The log likelihood function given a random sample of size n is given by

$$L = -n \ln(\pi) + n \ln(\alpha) + n(\partial\delta - \beta\mu) - \frac{1}{2} \sum_{i=1}^n \phi(x_i) + \beta \sum_{i=1}^n x_i + \sum_{i=1}^n K_1(\partial\alpha\phi(x_i)^{1/2})$$

The log likelihood function of the normal distribution,  $N(\mu, \sigma)$  given a sample of size n is given by

$$L = \sigma^{-n} (2\pi)^{-n/2} \exp \left[ -\frac{1}{2\sigma^2} \sum_{i=1}^n (x_i - \mu)^2 \right]$$

The maximization of the log-likelihood function is done numerically using an optimization algorithm. For further details about this, see (Myung, 2003). However, I have chosen to use the R-package.

### 3.4 Goodness of fit

There are various approaches for measuring the goodness-of-fit of a given model. These include the following.

#### 3.4.1 QQ-plots

We use the QQ-plot graphical technique for determining which distribution best fits the data set.

#### 3.4.2 Anderson-Darling test statistic:

$$AD = \max_{x \in R} \frac{|F_n(x) - F(x)|}{\sqrt{F(x)(1 - F(x))}}$$

Where,  $F_n(x) = (\text{no. of } x_i \leq x)/n$ , is the empirical cumulative distribution function and  $F(x)$  is the cumulative distribution function.

A smaller value of AD means that the empirical distribution and fitted distribution are closer.

### 3.5 Risk-neutral Option Pricing

We assume that the price  $B(t)$  of a risk-free asset satisfies the ordinary differential equation

$$dB(t) = rB(t)dt, \text{ where } r \geq 0 \text{ is the interest rate.}$$

By first *fundamental theorem of asset pricing*, if a *risk-neutral probability measure* exists, then there is no arbitrage. This risk-neutral probability is a martingale measure  $\mathbb{Q}$  that is equivalent to the original probability measure P and such that the underlying asset price is a  $\mathbb{Q}$  local martingale.

A *European call option* is the right but not obligation to buy a contingent claim at the *time of maturity* T to a fix *strike price* K. Thus the payoff function is given by

$$\max(S(T) - K, 0).$$

The *arbitrage-free value* of the option at time  $t < T$  can be defined as

$$C_t = e^{-r(T-t)} E^{\mathbb{Q}} \left[ \max(S(T) - K, 0) \right]$$

### 3.6 Option Pricing Using Fast Fourier Transform (FFT)

The European call option price will be based on the asset price process,  $S_t$ , with maturity time  $T$  and strike price  $K$ . Write  $k = \log(K)$  and  $s(T) = \log(S(T))$ .  $C_T(k)$  denote the option price and  $f_T$  the risk-neutral probability density function of price  $s_T$ .

The characteristic function of the density  $f_T$  is given by

$$\phi_T(u) = \int_{-\infty}^{\infty} e^{ius} f_T(s) ds. \tag{11}$$

The option value which is related to the risk-neutral density  $f_T$  is given by

$$C_T(k) = \int_k^{\infty} e^{-rT} (e^s - e^k) f_T(s) ds \tag{12}$$

Here  $C_T(k)$  is not square integrable because when  $k \rightarrow -\infty$  so that  $K \rightarrow 0$ , we have  $C_T \rightarrow S(0)$ . To obtain a square integrable function, we consider the modified price  $c_T(k)$  given by

$$c_T(k) = e^{\lambda k} C_T(k), \tag{13}$$

for a suitable  $\lambda > 0$ . The value  $\lambda$  affects the speed of convergence.

The Fourier transform of  $c_T(k)$  is defined by

$$\varphi_T(v) = \int_{-\infty}^{\infty} e^{ivk} c_T(k) dk. \tag{14}$$

We first develop an analytical expression for  $\varphi_T(v)$  in terms of characteristic function,  $\phi_T$ , and then obtain call prices numerically using the inverse transform

$$\begin{aligned} C_T(k) &= \frac{\exp(-\lambda k)}{2\Pi} \int_{-\infty}^{\infty} e^{-ivk} \varphi_T(v) dv \\ &= \frac{\exp(-\lambda k)}{\Pi} \int_0^{\infty} e^{-ivk} \varphi_T(v) dv \end{aligned} \tag{15}$$

$$\begin{aligned} \varphi_T(v) &= \int_{-\infty}^{\infty} e^{ivk} \int_k^{\infty} e^{\lambda k} e^{-rT} (e^s - e^k) f_T(s) ds \\ &= \int_{-\infty}^{\infty} e^{-rT} f_T(s) \int_{-\infty}^s (e^{s+\lambda k} - e^{(1+\lambda)k}) e^{ivk} dk ds \\ &= \int_{-\infty}^{\infty} e^{-rT} f_T(s) \left( \frac{e^{(\lambda+1+iv)s}}{\lambda+iv} - \frac{e^{(\lambda+1+iv)s}}{\lambda+1+iv} \right) ds \\ &= \frac{e^{-rT} \phi_T(v - (\lambda+1)i)}{\lambda^2 + \lambda - v^2 + i(2\lambda+1)v} \end{aligned} \tag{16}$$

Call values are determined by substituting (16) into (15) and performing the required integration. Since the FFT evaluates the integrand at  $v = 0$ , the use of  $\exp(\lambda k)$  is required. Therefore it is necessary to make an appropriate choice of the coefficient  $\lambda$ . Positive values of  $\lambda$  assist in the integrability of the modified call value over the negative log strike axis, but aggravate the same condition for the positive log strike direction, and hence

for it to be square-integrable as well, a sufficient condition is provided by  $\varphi(0)$  being finite provided that  $\phi_T(-(\lambda+1)i)$  is finite. From the definition of the characteristic function, this requires that

$$E[S_T^{\lambda+1}] < \infty \tag{17}$$

Carr and Madan suggest that, one may determine an upper bound on  $\lambda$  from the analytical expression for the characteristic function and the condition (17). One quarter of this upper bound serves as a good choice for  $\lambda$ , that is  $\lambda \approx 0.75$ .

At  $v = 0$  equation (15) becomes,

$$C_T(k) = \frac{\exp(-\lambda k)}{\Pi} \varphi_T(0)$$

$$\text{Where, } \varphi_T(0) = \frac{e^{-rT} \phi_T(-(\lambda+1)i)}{\lambda^2 + \lambda}$$

$$\text{Therefore, } C_T(k) = \frac{\exp(-\lambda k)}{\Pi} * \frac{e^{-rT} \phi_T(-(\lambda+1)i)}{\lambda^2 + \lambda}$$

The characteristic function of the log of  $S_T$ , which follows a NIG distribution, is given by

$$\phi_T(u) = \exp \left[ \ln \pi \Phi(g) + T \left[ r + \alpha^2 \sigma^2 - \alpha \sigma^2 \sqrt{\alpha^2 - iu} \right] \right]$$

$$\phi_T(-(\lambda+1)i) = \exp \left[ \ln \pi \Phi(g) + T \left[ r + \alpha^2 \sigma^2 - \alpha \sigma^2 \sqrt{\alpha^2 - (\lambda+1)} \right] \right]$$

The equation to get the option price of an NIG model is therefore,

$$C_T(k) = \frac{\exp(-\lambda k)}{\Pi} * \frac{\exp \left[ \ln \pi \Phi(g) + T \left[ r + \alpha^2 \sigma^2 - \alpha \sigma^2 \sqrt{\alpha^2 - (\lambda+1)} \right] \right]}{(\lambda^2 + \lambda)}$$

We now get the expression for the characteristic function of the normal distribution and use it to get the option price

The characteristic function of normal distribution is given by

$$\phi_T(u) = e^{i\mu u - \frac{1}{2}\sigma^2 u^2}$$

The Brownian motion is a type of Levy process. Therefore, under  $\square$ ,  $S_t^N$  is a Levy process with characteristic

triplet  $\left( \tilde{\mu}, c, \nu \right)$  and the distribution of  $S_1^N$  becomes  $s \left( \tilde{\mu}, \sigma, \psi \right)$ , where

$$\tilde{\mu} = r - \ln \psi \left( -\frac{\sigma^2}{2} \right)$$

The standard Brownian motion is  $N\left(0, \int_0^t \sigma^2 ds\right)$

Therefore,  $\phi_T(u) = e^{-\frac{1}{2} \int_0^T \sigma_t^2 u^2 dt}$

$$\phi_T(-(\lambda+1)i) = \exp\left[\ln \pi \Phi(h) + T \left[r - \frac{1}{2} \int_0^T \sigma_t^2 (\lambda+1)^2 dt\right]\right]$$

The option valuation for the normal distribution is given by

$$C_T(k) = \frac{\exp(-\lambda k)}{\Pi} * \frac{\exp\left[\ln \pi \Phi(h) + T \left[r - \frac{1}{2} \int_0^T \sigma_t^2 (\lambda+1)^2 dt\right]\right]}{(\lambda^2 + \lambda)}$$

**Remark:** We will use AM92 Actuarial tables to get the values of  $\Phi(g)$  and  $\Phi(h)$ .

#### IV. Application, Results and Conclusions

Data for analysis was sourced from [11], which is in the public domain. Codes for the main analysis appear in the Appendix. The results from the analysis are as follows.

##### 4.1 Stylized features

###### 4.1.1 Skewness and kurtosis

The skewness of log returns of price of carbon is -0.1212164. Since this value is near zero it is safe to say that our data is indeed symmetric. The value of kurtosis is -1.36154. This justifies the use of NIG levy process to model our data. The skewness and kurtosis of Gaussian distributions are 0 and 3 respectively.

###### 4.2 Parameter Estimation

Asymmetric Normal Inverse Gaussian distribution:

**Table 1:** Maximum Likelihood Estimates for Parameters:

	$\mu$	$\sigma$	$\beta$	$\alpha$
NIG	1.562073917	0.003563	-1.650997	12.358663
Normal	-0.0952422	0.44958767		

### 4.3 Q-Q Plot

#### Normal inverse Gaussian Q-Q Plot

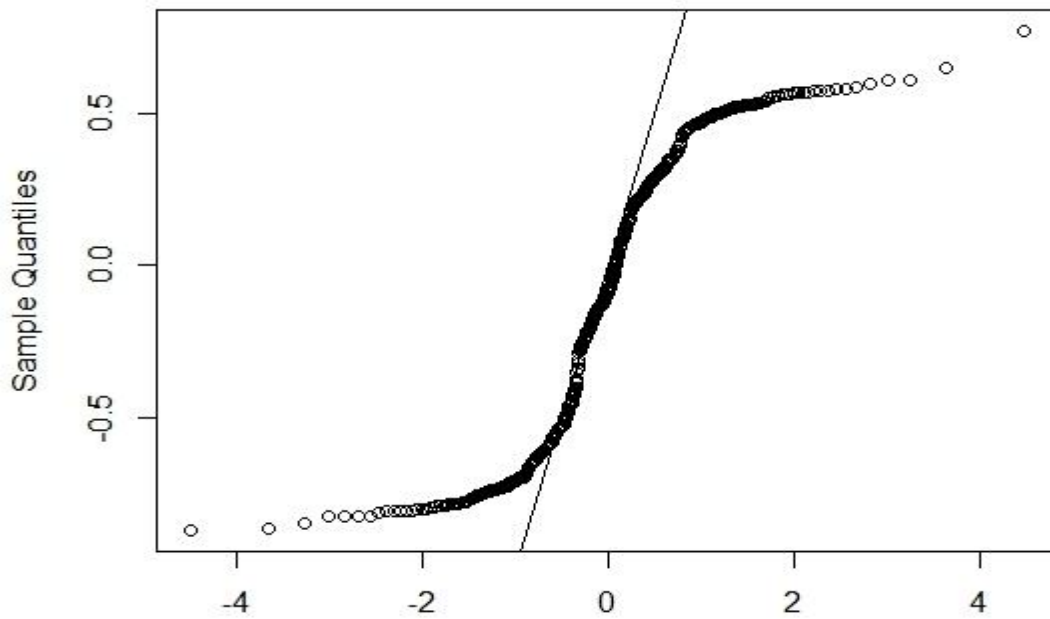


Figure 1.3: NIG QQ plot  
param = (0, 1, 1, 0, -0.5)

#### Normal Q-Q Plot

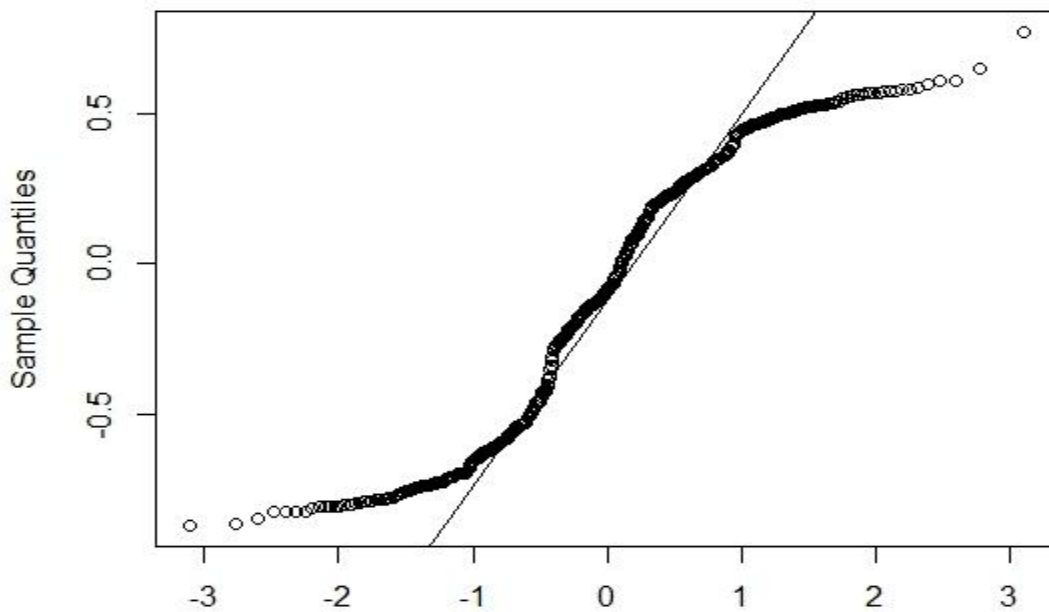


Figure 1.4: Normal QQ plot

The QQ-plots indicate that the empirical data fits much better to the NIG levy process than the Brownian motion.

**4.4 Anderson-Darling (AD) test Statistic:**

**Table 2:** AD statistic for NIG and Brownian Motion

	AD
NIG	131.7
Normal	208.5

The AD-statistic value is relatively smaller for the NIG Levy process than Brownian motion.

**4.5 Model Parameter estimates**

Suppose the strike price, K, is 20 Euros, 25 Euros or 30 Euros, T=4 (compliance phase),  $\Gamma_0 = 5$ ,  $\Pi = 3.14$  and  $r=0.05$ . The value of the call option using NIG model and Brownian motion are:

**Table 3 :** NIG model Parameter estimates

K	k	$C_T(k)$
20	2.9957322	1.2535
25	3.2188758	1.06
30	3.4011973	0.92

**Table 4 :** Brownian Motion Model Parameter estimates

K	k	$C_T(k)$
20	2.9957322	0.00806
25	3.2188758	0.00682
30	3.4011973	0.00595

The option prices in the NIG model are higher than those of the Brownian model with respect to the given strike prices. As the strike price increase, the value of the option decreases in both models.

**V. Conclusion**

The significant parameters in the NIG model are the  $\alpha$  and  $\sigma$ , while for the Brownian Motion model the significant parameter is  $\sigma$ . The NIG model has a better fit to data compared to the Brownian Motion model. Using the Fast Fourier transform, NIG model gives higher option prices than the Brownian motion.

**References**

- [1.] Anderson, T. W. and Darling, D.A. (1954). *A test of goodness of fit*. Journal of the American Statistical Association, 43, 26-37.
- [2.] Bu, Yongqiang (2007). *Option pricing using Levy Processes*. Chalmers tekniska hogskola. Chapman & Hall, New York.
- [3.] Cont, R. and Tankov, P. (2004) *Financial Modelling with Jump Processes*. Chapman & Hall, New York.
- [4.] Erik Bolviken and Fred Espen Benth(2000) *Quantification of Risk in Norwegian stokes via the Normal Inverse Gaussian distribution*. Proceedings of the AFIR 2000 Colloquium,Tromso, Norway, Vol. 8798, 2000.
- [5.] Hamza, Kais et al( 2015) *Option pricing for Symmetric Levy Returns with Applications*. Asia-Pacific Financial Markets. 22, 1, 27-52
- [6.] Jan Seifert, Marliese Uhrig-Homburg and Michael Wagner(2008). *Dynamic Behaviour of Carbon Spot Prices*. Journal of Environmental Economics and Management. 24, 180-194
- [7.] Julien Chevallier and Benoit Sevi (2014) *On the Stochastic Properties of Carbon Futures Prices*. Environmental and Resource Economics. 58,1, 127-153

- [8.] Kitchen, Cliff (2009). *Normal Inverse Gaussian (NIG) Process with Applications in Mathematical Finance*. *Mathematical and Computational Finance* . 41(2) 25-32
- [9.] Rene Carmona and Juri Hinz(2011) *Risk-neutral Models for Emission Allowance Prices and Option Valuation*. *Management Science*. 57(8) 1453-1468
- [10.] Saebo, Karsten Krog (2009) Pricing Exotic Options with the Normal Inverse Gaussian Market Model using Numerical Path Integration. Norwegian University of Science and Technology
- [11.] Data Link: <http://www.investing.com/commodities/carbon-emissions-historical-data>

#### Appendix: R codes used in the Analysis

```
Carbon = read.csv(file.choose())
```

```
Carbon
```

```
Price <- carbon$Price
```

```
Price
```

```
Plot(price, xlab="Fig1.1:carbon prices")
```

```
Plot (log_returns4, type="l", xlab="Figure 2.2: Log returns of carbon prices", ylab = "Log returns ")
```

```
Log_returns4 <- diff(log(price), lag=364 )
```

```
Log_returns4
```

```
par(mfrow=c(1,2))
```

```
qqnig(log_returns4, mu=0, delta=1, alpha=1, beta=0, xlab="Figure 1.3: NIG QQ plot")
```

```
qqnorm(log_returns4, xlab = " Figure 1.4 : Normal QQ plot ")
```

```
qqline (log_returns4)
```

```
y1
```

```
ad.test(y1)
```

# Hypergiant –conducting nanogranular compound materials, as IR-photon detectors for Boson-current transport at room temperature with $GA/cm^2$ current carrying capability

Hans W.P. Koops <sup>a)</sup>

HaWilKo GmbH 64372 Ober-Ramstadt, Ernst Ludwig Straße 16, Germany

## I. Introduction

In vacuum nano electronics different electron sources are used. They usually consist of hot or cold zirconia, tungsten, or carbon tips, the latter being in diamond or nanotube form. Electron sources of a special composite of precious metal crystals, which are embedded in a fullerene matrix, were first developed in 1992 at the Research Institute of Deutsche Telekom FTZ in Darmstadt, Germany. With those very high emission current densities were achieved and were brought to applications. Outstanding room temperature conductivities were achieved with these nanogranular composite materials, and are presented here along with a model to explain the measured data,

## II. Currents from conventional emitters

Typical metallic or even single carbon (carbon nanotube) emitters only start their current field emission above several 100 V and never reach emission currents of mA. Although the geometries of these conventional and the new emitter tips are very similar, in the case of pure platinum or carbon spikes, the work function for platinum of the electrons is 5.4 eV and for carbon 4.8 eV. Therefore, very high extraction voltages are always required with these field emitters, and the maximum emission currents are at 10  $\mu A$  for Pt. Carbon nanotubes reach 0.1  $\mu A$ , since they vaporize their carbon atoms from the tip due to the ohm resistance of the nanotube [1]. Also, metal field emitter tips do not reach current emissions greater than 10  $\mu A$  due to the internal resistance of the wires. These then melt due to the high resistance at elevated temperature. Successful deposition experiments arrive with carbonyls of the metals, preferably tungsten hexa-carbonyl. However, these compounds showed emissions as known from standard field emitters, i.e. they gave a maximum emission current of 10  $\mu A$ , and required high extraction voltages of > 1 kV, see also [2].

## III. Nanogranular composites for high-performance electron sources

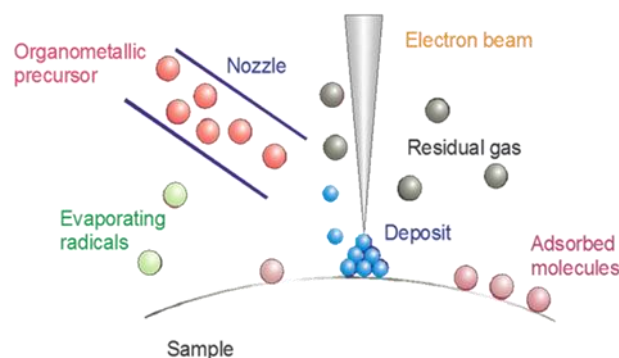


Figure 1: Deposition of emitter tips using nano-granular compound materials.

Organometallic compounds have been used to prepare the electron sources described above. For this purpose, the selected organo-metallic materials were supplied by commercial manufacturers<sup>[3]</sup>, which have a low vapor

pressure at room temperature. They were supplied from a reservoir in a molecular beam to the deposition site by means of a cannula, see figure 1. The nanogranular emitters grow due to

a) Hans W.P. Koops, HaWilKo GmbH Ober-Ramstadt, e-mail: [hans.koops@t-online.de](mailto:hans.koops@t-online.de) 18. 3.2018

the electron scattering in the heavy metals to a relatively blunt tip of about 10 nm radius of curvature. The material is not monocrystalline - as in conventional emitters - but grows under the high dose of the primary beam to metal crystals of 2 to 4 nm diameters, which are embedded in a fullerene crystal matrix having 1 to 2 nm diameters. During the growth the metal nanocrystals solidify at 500°C and are encapsulated by the fullerenes at 150 °C, see figure 2.

The tip material is polycrystalline. It is composed of very small metal crystals, each containing about 800 metal atoms embedded in an enveloping phase of fullerenes (Bucky-balls).

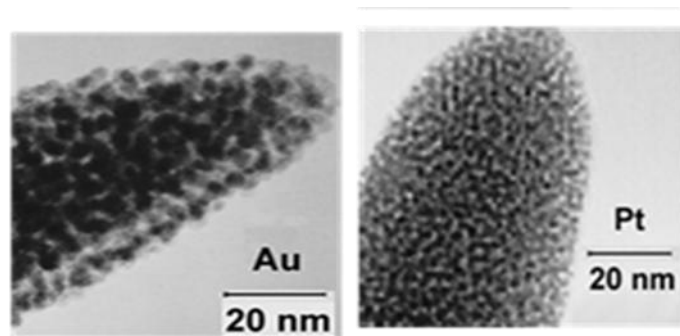


Fig. 2. Nanogranular compound field emitter tips. Left: Gold with crystal diameters of 4 nm, grown with Gold-Acetylacetonate-tri-methyl. Right: Platinum, grown from cyclopentadienyl-platinum-tri-methyl methyl to diameters of 2 nm. Both experiments: 20 kV electrons, 1 nA electron current, focused to 4 nm spot. ( 300 kV TEM images by MPI Halle ).

The deposited tips, which were used for the photographs in the TEM were deposited in the JEOL 840 SEM at Telekom with nA electron current on edges of standing mounted copper object carrier grids. This allowed to image the tips in horizontal position in the TEM, and avoided the scattering contrast contribution of a carrier foil.

To understand the materials better, work function measurements were performed, see figure 3, left. They resulted in activation energies for variable range hopping for Pt/C and Au/C in the meV range! This result indicated that the nanogranular compound material is well suited for energy harvesting in the IR region. Also the construction of the compound materials with many layers of crystals, having the same energy gaps for excitonic energy levels enhances the sensitivity of the material to absorb light of all frequencies from IR to UV! Figure 3, right, shows a white-light optical image in reflection. On an silicon base coated with SiO<sub>2</sub> gold contact areas were structured, which allowed 3 lines (green) to be deposited with 20 kV electrons. Using the Pt-cyclopentadienyl-tri-methyl-methyl precursor 3 bridges were deposited, which are broadened by the forward and back scattered electrons by additional deposition. This material looks black in the light microscope, indicating that all photons of the white spectrum from the lamp were absorbed by the nanocrystalline deposit.

As a result, the required extraction voltage for field electron emission was much lower than with metal single crystal emitter tips. Thus, gold / carbon nanogranular emitters, delivered the first emitted electrons starting at 8 V, and terminated the emission at extraction voltages of 24 V at an emission current near 1 mA. The emitter-extractor distance was less than 0.8 μm, see figure 4. The same applies to the Pt/C emitters, which began to emit at 15 V and ended at 75 V with an emission current of 1.4 mA or an emission current density of 1.4 GA / cm<sup>2</sup>.

Electrons emanating from the emitter tip were coherent, as seen in the far field, by registering several patterns of interference fringes. This measurement confirms that the electrons emitted from the field emitters are coherent, indicating that they come from coherent bosons existing in the tip material [4].

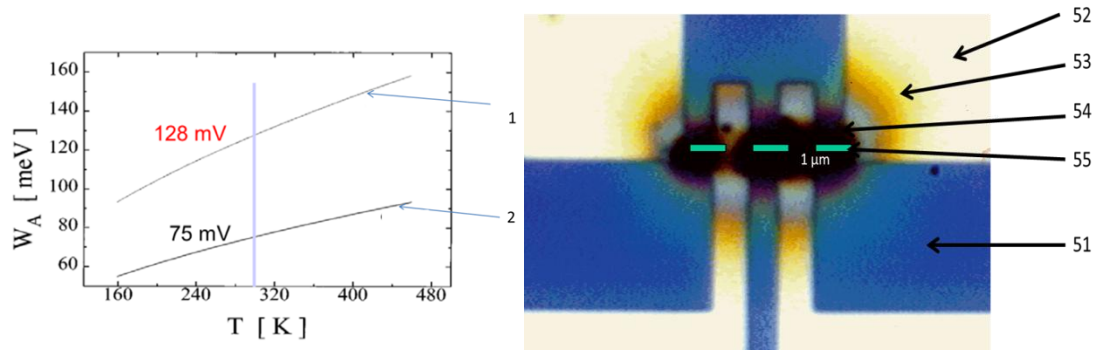


Fig. 3. Left: Activation energies for variable range hopping for Pt/C (1) and Au/C (2) [5]. Right: Optical photograph with white light illumination. Optical sensitivity of a line deposited with Pt/C (55) green: beam trace. Back scattered nanocrystalline deposit: black (54); blue area (51): SiO<sub>2</sub> on Si base material. Interference colors(53): insulating deposit. White areas: (52) Gold contact layers).

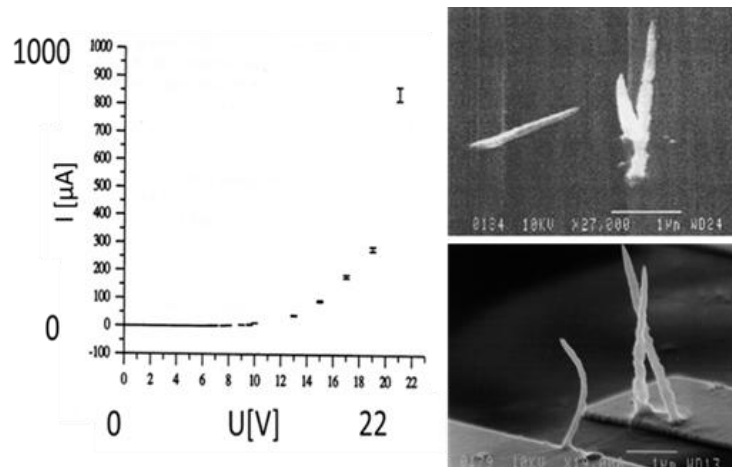


Fig. 4: Left: Au/C emission curve. Right Top: Diode- Source before the measurement: left: emitter, right extractor in x-shape. Right Bottom: Structure obtained, after the emission curve stopped [6]. The bent form of the emitter originated from implantation of water molecule ions sputtered from the anode and implanted at the cathode side facing the anode. This implantation can be prevented by using a potential saddle point between cathode and anode with a potential higher than the anode potential. This prolongs the lifetime of the emitter [7, 8].

#### IV. Model to explain the hyper giant emission current densities

One explanation was formulated by Inosov et al. in 2010 of the superconductors using Cooper pairs and their high currents of up to 1 MA / cm<sup>2</sup> in wires, which are cooled to 40 K[9]. This provided the impetus for the formulation of a model to explain the hyper giant current carrying capacity of the novel nanogranular composite materials. Inosov and colleagues recognized that the Cooper pairs being formed from two electrons having antiparallel spin can reside as Bosons at the same energy level. This allows current densities of 1 MA/cm<sup>2</sup> in the material.

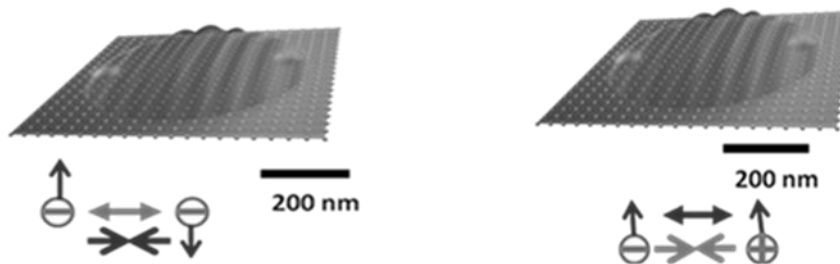


Figure 5: Left: Cooper pair, 2 charges repel, but antiparallel spins attract and balance the boson. Right: Koops pair, electron (-) and hole (+) attract, but the parallel spins repel and stabilize the Boson to a diameter of 600 nm.

The only difference between Cooper pairs and Koops pairs is in the sign of the charges and for the magnetic forces.

This is predicted by Maxwell's theory. However, for Cooper pairs cooling with liquid nitrogen to at least 40 K was required.

But our experiments with Koops pairs were performed at room temperature: 300 K!

Considering that by electron beam obtained Au/C or Pt/C deposits are nanocrystalline composite materials, with crystallite diameters of Pt (2 nm) or Au (4 nm), each encased in a layer of fullerene crystals. This means that now 2 conductive phases touch each other. Therefore, it is concluded that 2 work functions (Pt: 5.4 eV or Gold: 5.0 eV and Carbon: 4.8 V) are in contact and immediately form a common average Fermi level (Pt / C: 5.1 eV, and Au / C: 4.9 eV) into which the carbon must give up its electrons and thus the platinum or the gold is negatively charged. The energy states above the common Fermi level are empty, and extend through the whole composite matter.

At room temperature, electrons in the adjacent metals are excited by the Maxwell energy distribution in the conduction band, and they can occupy the empty energy levels in the Pt / C or Au / C material and immediately form after Bose Bosons from electron and hole with parallel spin. This behavior is made possible by the fact that crystals with a diameter of less than 5 nm can no longer carry phonons [10, 11]. These Bosons are at the same energy level, and are coherent, and can be up to  $10^{28}$  / cm<sup>2</sup> in number. And since the material is no longer a pure metal that obeys the Fermi energy distribution, with only 2 electrons per level, but it is now composed by Bosons, which have a dipole moment (+, -) with many particles in the same level, similar to lasers. For data comparison: high temperature super conductors (HTc) reach at 40 K with titanium doped magnesium-di-boride < 1 MA/cm<sup>2</sup> ! [see table 1: 17], but the nanogranular composite materials reach up to 1 GA/cm<sup>2</sup>.

## V. History of the discovery of nanogranular compound materials for electron sources and other applications.

Material combination of emitters	Maximum obtained current carrying capability	Temperature T [°C]	Investigation at	Citation
Nanogranular compound materials:				
Au/C	2 MA/cm <sup>2</sup> , 10 <sup>3</sup> MA/cm <sup>2</sup> (tip)	RT	Measured in UHV ( TU Darmstadt)	[12]
Pt/C	2 MA/cm <sup>2</sup>	RT	Measured in UHV ( TU Darmstadt)	[13]
Pt/C	15 MA/cm <sup>2</sup>	RT	Measured at wire archUniv. Maryland USA	[14]
Pt/C	10 MA/cm <sup>2</sup>	RT	Measured in HV (DTAG)	[15]
Pt/C	100 MA/cm <sup>2</sup>	RT	Measured in HV (NaWoTec, D)	[16]
Me/Fullerene	>50 MA/cm <sup>2</sup>	20	Metal in nanogranular matrix, Embedded (Me)	[17]
For comparison: High Temperature Superconductors (HTc):				
TitaniumdopedMagnesiumdi-boride	<1MA/cm <sup>2</sup>	--233,15	Spektrum d. Wissenschaft. 7. 2005	[18]

Table 1: Emission current densities from field-emitters from nanogranular composite materials (FEBIP: Focused Electron Beam Induced Processing), see publications by several authors 1994 to 2005.

## VI. But the Bosons cannot move!

The Bosons can be moved only by applying a field gradient of an electric field along the wire. When they reach the end of the wire, the Bosons disintegrate into an electron and a hole. The electron escapes from the substance and goes into vacuum (emission of electrons) or into the conductor of the terminal by tunneling into the conduction band. This explains the electron emission, but also why the work function is so low, and why the current is so much higher than with the emission of electrons from a metal after the Fermi Dirac distribution. Therefore, this electron emission is the solution to the mystery of the hyper giant-current density as it was

measured by our group at FTZ with these nanogranular composite emitter tips. It was also measured at the Helmholtz Institute KIT – KNMF in Karlsruhe, Germany, see figure 6.

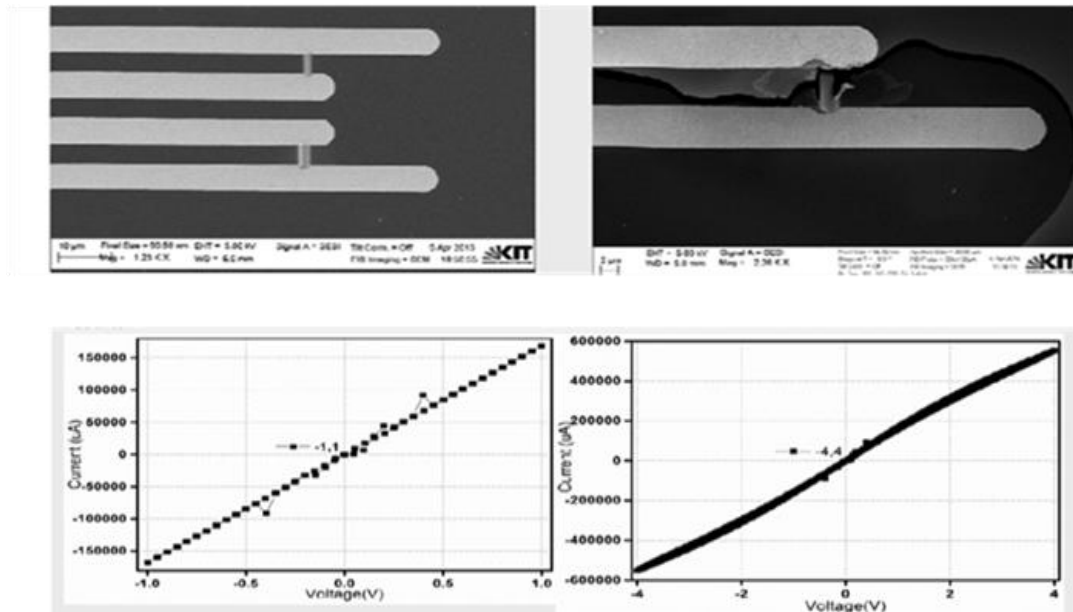


Fig. 6: Top left: Measurement setup to determine the current carrying capability of Pt/C deposit between platinum conducting lines. Top right: an overloaded deposit. The Pt- conducting lines melt but not the Pt/C deposit under investigation. The lower graphs show I/V curves. Left: the current obtained between + 1 V and – 1 V. right: for -4 V to + 4 V. A current up to 0,6 A was possible ( with friendly allowance of KIT/ KNMF).[19]

Also, by multiplying the emitter tips in parallel, we had to learn that the size of the matching connecting surface of the structure to the deposited pure metal is limited by its current carrying capacity. By friendly cooperation with Mr. A. Rudzinski of the company RAITH, Germany, we were able to make electrical measurements of the device, see Figure 7.

To increase the available currents, a plurality of emitter tips were deposited in parallel at intervals on cone-shaped deposited contacts on a gold conductor end. When measuring the emission currents from 5 emitters connected in parallel, an emission starting at 15 volts was measured with an increase up to 135  $\mu\text{A}$  total current, which then stopped and completely disappeared at 80  $\mu\text{A}$ , see Figure 7. The explanation for the stop is as follows: Gold as a patterning material can carry 250  $\text{kA}/\text{cm}^2$ . The measured current of 135  $\mu\text{A}$  corresponds for the 5 emitter sets already a ten-fold overload and therefore results in melting of the electron emitters. The nanogranular compound materials demand to first build a large area as an connection sheet to the underlying metal, and to deposit only then on top of this structure the electron emitters.

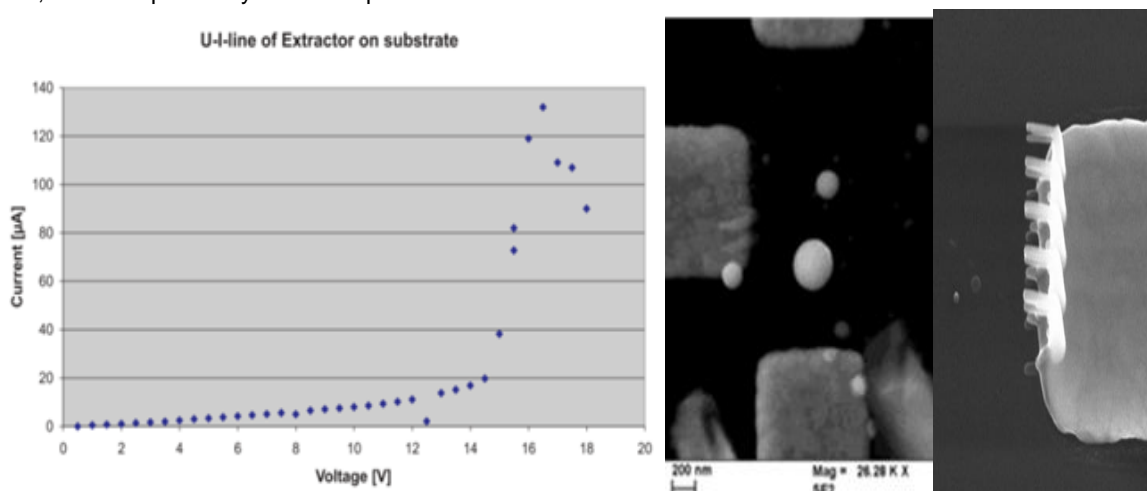


Fig. 7: I/V curve for multiple parallel emitters used to increase the emitted current. Center structure after raising the extraction voltage by 2 Volts, the base material did melt. Right: Emitter structure before starting the experiment

Other experiments showed, that the deposited nanogranular compound material has 0 Ohm resistance, but is controlled in its conductivity by the diameter and property of the contact material only [20].

### VII. Koops-GranMat can be applied for harvesting of Greenhouse gas emission in the IR

NASA recorded in a 10 years measurement the in 2009 quoted data-average in  $W/m^2$  [21].

In addition to the sunlight, which sends  $160 W/m^2$  to the earth during the day, the green-house gas molecules in the upper atmosphere send in the infrared window of the earth's atmosphere Infra-Red photons with  $340 W/m^2$  directly to earth during the day and the night. This is a 4 fold energy supply compared to that in the visible spectrum. Greenhouse gases emit in the near IR range, e.g. at 128 meV ( Pt/C). We can harvest in the near IR the emitted energy with the Koops-GranMat® detector. This is the region, where the atmosphere of the earth is transmitting the IR radiation to the earth with  $340 W/m^2$ , in day and at night. The atmosphere has a high transmission region at  $5 \mu m$  to  $10 \mu m$ , where no absorption loss hinders this energy supply at day and at night.

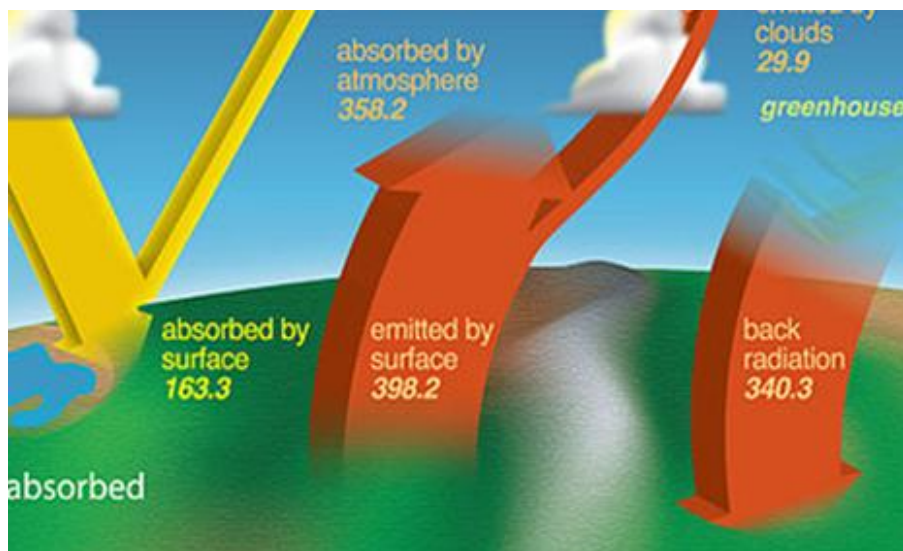


Fig. 8: The earth-near space delivers a lot of greenhouse energy to the earth, day and night.

The water containing atmosphere does not absorb the IR radiation around 7 to 10  $\mu m$ .

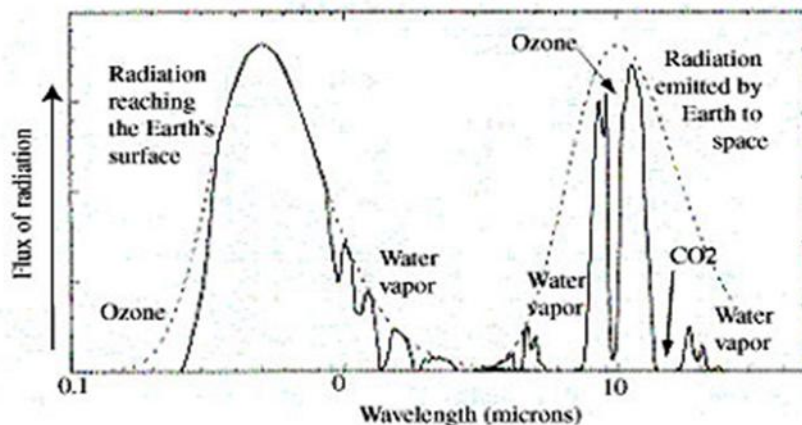


Fig. 9: The IR reception of Pt/C is in the gap before 10  $\mu m$ , where there is no absorption.

This energy can be absorbed with the panels or films, which are coated with Boson field gradient materials. The energy harvesting requires only a field-gradient in the receiver layers, to move the electrical energy to the user. See figure 9 and 10. To harvest the energy from the green-house gases in the earth atmosphere sheets of glass or polymers can be coated with electron-beam induced deposition materials. Presently Pt/C or Au/C nanogranular compound materials are known. However less expensive materials are also possible, which have a low bandgap, like 0.128 eV for Pt/C compound layers.

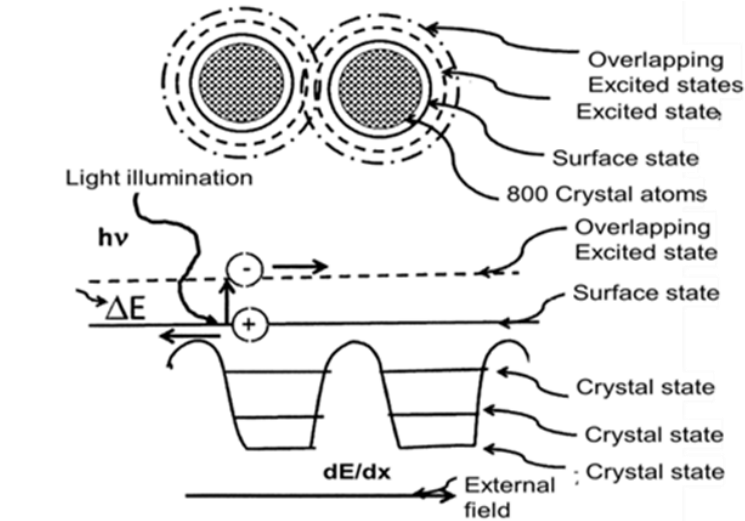


Fig.10. Principle of energy harvesting from the green-house emission using nanogranular compound materials. Since a 2 materials mixture is used, the 2 materials form a common Fermi-level. The Pt-material takes the electrons from the Fullerene crystals, which have therefore holes. The incoming radiation excites the electrons in the Fermi-Level to the level with the holes. There electrons and holes form Bosons in a very high density. They can be moved by an external dipole moment and finally deliver electrons to the outside world for work.

Nano-composit materials, e.g. Pt/C are sensitive in the IR light and can harvest all day and night the IR- light, which is emitted by the Green-House – gases in the upper atmosphere. By switching on a field gradient at the rim of the Koops-GranMat® detector layer the in Bosons stored energy is at the end of the layer released as electrons to the customer.

This material unifies the radiation detector, the storage device, and the energy supply, see figure 11. IR-Solar-receivers are especially useful in areas having a low density of population, but need to use electrical machines like pumps, cars and other tools.

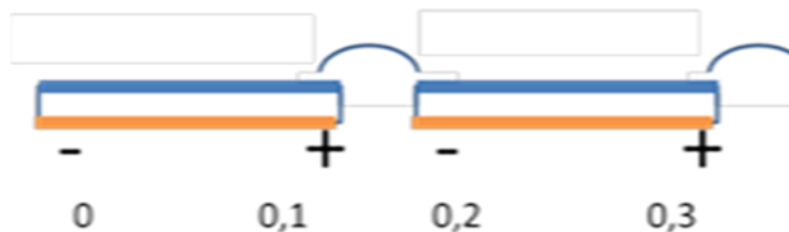


Fig. 11: To move Bosons a field gradient is required, which can propel the dipoles of the Bosons to the end of the field gradient, where they can decay and deliver the charge to a user.

The current supply can be controlled by adjusting the static field gradients or switching them on or off. The principle has been shown, in the experimental stage. Now a larger area layer of 1 cm<sup>2</sup> is under construction for demonstration.

Later presently existing glass coating machines, which deposit by ion bombardment the coating layers on glass or polymer sheets, can be used by replacing the Sputter-sources with ions by field-emission array electron sources, which deposit the nanocrystalline detector layers from organometallic precursor gases to absorb the IR radiation and convert this finally to electrons or current.

## VIII. Conclusions

Nanogranular compound materials offer a possible solution to absorb energy from the space in the earth atmosphere without interruption by day and at night. The green-house gas emission is the powerful source of 340W/m<sup>2</sup> during day and night. Large area detectors and storage devices are possible, which are far more efficient than present Silicon solar energy panels. The fabrication is possible by small changes in today's glass coating systems. It will be a revolution for the earth energy budget without the need to burn coal or plants. All this energy comes in the end from the sun and the space.

## References

- 
- [<sup>1</sup>] W.I. Milne and M.T. Cole: Carbon Nanotubes for Field Emission Applications, Engineering Department, Electrical Engineering Division, University of Cambridge, IP3 Technical Digest of IVNC (2012) 12.
- [<sup>2</sup>] H.W.P. Koops, “Hyperriesig leitende nanogranulare Materialien“VIP Vol.30, Nr. 1 35-39 , Wiley VCH Verlag, Weinheim, February 2018 in German , DOI: 10.1002/vipr. 201 800671
- [<sup>3</sup>] STREM Chemicals Europe
- [<sup>4</sup>] K. Murakami, F.Wakaya, M. Takai, J. Vac. Sci. Technol.B. 25 (4) (2007) 1310-1314
- [<sup>5</sup>] H.W.P. Koops, A. Kaya, M. Weber, ”Fabrication and characterization of Platinum Nanocrystalline Material Grown by Electron Beam Induced Deposition”, J. Vac. Sci. Technol. B 13(6) Nov/Dec) (1995) 2400-2403
- [<sup>6</sup>] J. Kretz, M. Rudolph, M. Weber, H.W.P. Koops, "Three Dimensional Structurization by Additive Lithography, Analysis of Deposits using TEM and EDX, and Application for Field Emitter Tips"; Microelectronic Engineering 23(1994)477-481.
- [<sup>7</sup>] H.G. König, H.Koops, Proc. Int. Conf. Microcircuit Engineering, Berlin 1984, Academic Press ed.: A. Heuberger, H. Beneking (1995) 195-202.
- [<sup>8</sup>] B. Yanko, Tectronix Patent 1978 DPA Nr. 27 38 928
- [<sup>9</sup>] D. S. Inosov et al.: Normal-state spin dynamics and temperature-dependent spin-resonance energy in optimally doped BaFe<sub>1.85</sub>Co<sub>0.15</sub>As<sub>2</sub>, Nature Physics Vol. 6 (2010) 178-181.
- [<sup>10</sup>] H. Lamb, “On the Vibration of an elastic Sphere”, Proceedings of the London Mathematical Society, Vol. 13, No.1, 1882, pp 189-212. Doi 10.1112/plms/s1-13.1.189
- [<sup>11</sup>] M. R. Geller et al. PhysicaB 316-317 ( 2002) 430-433
- [<sup>12</sup>] H.W.P Koops, et al., Review article on FEBIP: Jpn. J. Appl. Phys. 1994, 33, 7099-7107
- [<sup>13</sup>] H.W.P. Koops, C. Schössler, A. Kaya, M. Weber, "Conductive dots, wires and Super-tips for field electron emitters produced by electron-beam induced deposition on samples having increased temperature" J. Vac. Sci. Technol. B14(6) (1996) 4105
- [<sup>14</sup>] K. Edinger; Rangelow I.W., Gottszalk, T.: J. Vac. Sci. Technol. 2001, B19, 2856-2860.
- [<sup>15</sup>] Floreani F; Koops H.W.P.; Elsässer W.; Nuclear Instruments and Methods in Physics Research A 2002, 488 – 492.

[<sup>16</sup>] J. Sellmair, NaWoTec GmbH, Rossdorf; private Note, 2005

[<sup>17</sup>] H.W.P.Koops, Journal of Coating Science and Technology, 2016, 3, 50-55, DOI:<http://dx.doi.org/10.6000/2369-3355.2016.03.02.1>.

[<sup>18</sup>] P.S. Canfield, D. Budko, im Spektrum der Wissenschaft Juni 2005, Seite 56.

[<sup>19</sup>] A. Machanda, Research Report at Karlsruhe Nano Micro Facility (KNMF) at the Karlsruhe Institute of Technology (KIT) 2016.

[<sup>20</sup>] Hans W.P. Koops, I.R. Rangelow, “Contact and Line Resistivity in Nanogranular Compound Materials Fabricated with Focused Electron Beam Induced Processing”, IVNC 2017, Regensburg Technical Digest,

[<sup>21</sup>] "Energy Budget of the Earth" of NASA, Leob et al. J. Clim, 2009, Treuberth et al. BAMS. 2009, NP-2010-05-265-LaRC

# A BBO-based algorithm for the non-convex economic/environmental dispatch

Asseri Ali Amer.M<sup>1</sup>, Marouani Ismail.T<sup>1</sup>

Electrical department, College Technology of Jeddah. KINGDOM OF SAUDI ARABIA  
aalasiri@tvtc.gov.sa ismailmarouani@yahoo.fr

## ABSTRACT

The problem of power system optimization has become a deciding factor in electrical power system engineering practice with emphasis on cost and emission reduction. The economic emission dispatch (EED) problem has been addressed in this paper using a Biogeography-based optimization (BBO). The BBO is inspired by geographical distribution of species within islands. This optimization algorithm works on the basis of two concepts-migration and mutation. In this paper a non-uniform mutation operator has been employed. The proposed technique shows better diversified search process and hence finds solutions more accurately with high convergence rate. The BBO with new mutation operator is tested on ten unit system. The comparison which is based on efficiency, reliability and accuracy shows that proposed mutation operator is competitive to the present one.

**Keywords**— *Economic emission dispatch (EED); Biogeography based optimization; Mutation operator.*

## I. INTRODUCTION

Electricity, like all energy forms or vectors generates environmental, economic and social impacts that are trying to limit. One of the challenges for the 21st century is that of production from clean, reliable, safe and renewable resources that can replace thermal and nuclear power plants. In this context, some states are introducing environmental policies to encourage electricity producers to reduce their greenhouse gas emissions and thus their direct or indirect contributions to climate change. For thermal energy, gas, oil and coal are fossil sources. It will come well on a day when their quantity will be restricted. In addition, the use of these fossil fuels leads to greater pollution, despite the measures taken (denitrification, desulphurization). To these harmful effects is added the rising cost of these different sources. It is in this axis that the content of our work lies, in order to reduce the emission of pollutant gas and the cost function of different sources simultaneously.

Several research considered the classic EED problem where the cost of production function of each thermal unit is approximated by a quadratic function [1-2]. While, modern systems are with units that have prohibited areas of operation (POZ) due to physical operation limitations. In addition, the practical problem of EED includes valve load effects (VPLE) in the cost function. These additional constraints make the problem with a high nonlinear and discontinuous objective function. For this reason, the traditional optimization techniques proposed in the literature, such as linear programming [3] Newton's methods [4] and lambda iteration [5] can not achieve the best solution.

In the past years, a number of approaches have been developed for solving this problem using classical methods like dynamic programming [6] and interior point [7] methods have been used to solve the static EED. Among metaheuristic-based optimization techniques, genetic algorithm [8], particle swarm optimization [9], simulated annealing [10-11], artificial bee colony (ABC) [12], tabu search [13], differential evolution [14] and bacterial foraging [15] have been suggested for solving the EED problem.

Recently, a new, easy-to-implement, robust evolutionary algorithm has been introduced known as Optimization based on biogeography (BBO) algorithm. This Optimization based on biogeography

(BBO) algorithm introduced by Simon [16], is one approach that has been used to find an optimal solution in numerical optimization problems. The BBO algorithm based on biogeography concept, is inspired by the principle of the movement of species, depends mainly on the topographical characteristics of the space considered called habitat and time.

## II. PROBLEM FORMULATION

In this EED problem, two objective functions to be minimized simultaneously, which are the total emission and the total cost of the fuel in order to find the power production of the thermal power plants according to expected load demands. The description of objectives and constraints is as follows.

In this EED problem, two objective functions to be minimized simultaneously, which are the total emission and the total cost of the fuel in order to find the power production of the thermal power plants according to expected load demands. The description of objectives and constraints is as follows.

### A. Objective functions

The higher nonlinearity due to the VPLE shown in FIG. 1 which has been neglected in conventional methods, and which is caused by the sequential operation of thermal units with multi-steam intake valves, is considered constrained in this study. For this reason, a sinusoidal form will be included in the non-convex total cost function expressed in (\$ / h), as shown in equation (1). The total emission in (ton / h) is described by equation (2) corresponding to the second objective.

$$C_T = \sum_{i=1}^N a_i + b_i P_i + c_i P_i^2 + \left| d_i \sin \left\{ e_i (P_i^{\min} - P_i) \right\} \right| \quad (1)$$

$$E_T = \sum_{i=1}^N \alpha_i + \beta_i P_i + \gamma_i P_i^2 + \eta_i \exp(\lambda_i P_i) \quad (2)$$

Where,

$a_i, b_i, c_i, d_i$  and  $e_i$  are the cost coefficients of the  $i$ -th unit. While,  $\alpha_i, \beta_i, \gamma_i, \eta_i$  and  $\lambda_i$  are the emission coefficients.  $P_i$  is the output power in MW at the the  $i$ -th unit.

In our study, the EED bi-objective problem is converted to a mono-objective optimization problem [17], as it is considered in several works. Using the price penalty factor (PPF) method, equation (3) describes the combined economic emission goal function  $F_T$  expressed as follows

$$F_T = \mu C_T + (1 - \mu) \lambda E_T \quad (3)$$

Where,  $\mu = rand(0,1)$ . The generated value of optimal solution, which can be a candidate solution in the Pareto front, is obtained by minimizing the  $F_T$  function for each value of  $\mu$ .  $\lambda$  is the average of the PPF of all thermal units. The PPF of the  $i$ -th unit is the ratio between its fuel cost and its emission for a maximum production capacity, described by equation (4).

$$PPF_i = \frac{C_{i_{\max}}}{E_{i_{\max}}} \quad (4)$$

### B. Problem constraints

The resolution of the problem EED is obtained by minimizing the  $F_T$  function that is defined by equation (3) subject to the following constraints.

- Generation capacity

Depending on the unit design, the output active power of each unit must fall between its minimum and maximum limits respectively  $P_i^{\min}$  and  $P_i^{\max}$

$$P_i^{\min} \leq P_i \leq P_i^{\max}, i = 1, \dots, N \quad (5)$$

- Power balance constraints

Respecting the balance of power constraints given by equation (6), the total electricity production must cover the total power required more total transmission losses  $P_L$ .

$$\sum_{i=1}^N P_i - P_D - P_L = 0 \quad (6)$$

Where  $P_L$  can be calculated using constant loss formula [18], as given below.

$$P_L = \sum_{i=1}^N \sum_{j=1}^N P_i B_{ij} P_j + \sum_{i=1}^N B_{oi} P_i + B_{oo} \quad (7)$$

Where,  $B_{ij}$ ,  $B_{oi}$ ,  $B_{oo}$  are the loss parameters also called  $B$ -coefficients.

- POZ constraints

The POZ constraints are described as follows.

$$P_i \in \begin{cases} P_i^{\min} \leq P_i \leq P_{i,1}^{\text{down}} \\ P_{i,k-1}^{\text{up}} \leq P_i \leq P_{i,k}^{\text{down}} \\ P_{i,z_i}^{\text{up}} \leq P_i \leq P_i^{\max} \end{cases}, k = 2, \dots, z_i \quad (8)$$

Where,  $P_{i,k}^{\text{down}}$  and  $P_{i,k}^{\text{up}}$  are down and up bounds of POZ number  $k$ .  $z_i$  is the number of POZ for the  $i$ -th unit due to the vibrations in the shaft or other machine faults.

This is explained in Figure 2 which illustrates the fuel cost function for a typical thermal unit with POZ constraints. Where, the machine has discontinuous input-output characteristics [19]. Equation (9) describes the minimum and maximum limits of power generation  $P_i$  of the  $i$ -th unit taking into account the production capacity and POZ constraints.

$$P_i \in \begin{cases} P_i^{\min} \leq P_i \leq \min(P_i^{\max}, P_{i,1}^{\text{down}}) \\ \max(P_i^{\min}, P_{i,k-1}^{\text{up}}) \leq P_i \leq \min(P_i^{\max}, P_{i,k}^{\text{down}}) \\ \max(P_i^{\min}, P_{i,z_i}^{\text{up}}) \leq P_i \leq P_i^{\max} \end{cases}, k = 2, \dots, z_i \quad (9)$$

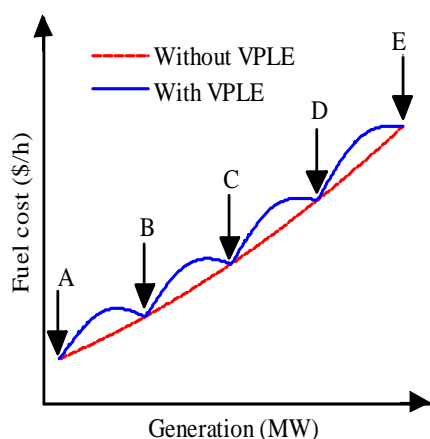


Figure 1. Fuel Cost Function with Five Valves (A, B, C, D, E)

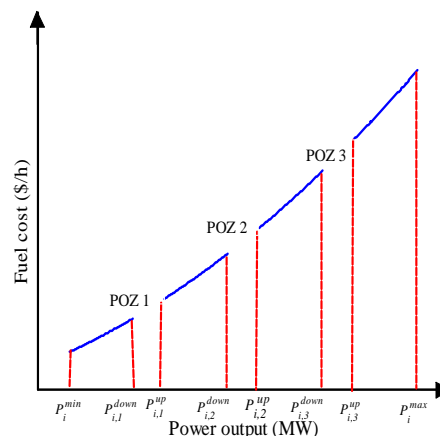


Figure 2. Cost function for a thermal unit with POZ constraints

### III. PROPOSED ALGORITHM WITH MUTATION

Optimization based on biogeography (BBO) is a new algorithm inspired by the principle of the movement of species, introduced by Simon [16]. This algorithm depends mainly on the topographical characteristics of the space considered called habitat and time. Figure 3 explains immigration and species migration. It can be seen that the  $S_{max}$  habitat capacity is reached for one of zero immigration and the immigration rate  $\lambda$  is maximum when no species in the habitat and decreases the habitat will be more congested. Whereas the emigration rate  $\mu$  is zero for the empty habitat. On the other hand, species migrate when the habitat is congested to find other suitable residences. Therefore, the emigration rate of species reaches its maximum value  $E$  when the number of species in habitat  $S$  equals to  $S_{max}$ .

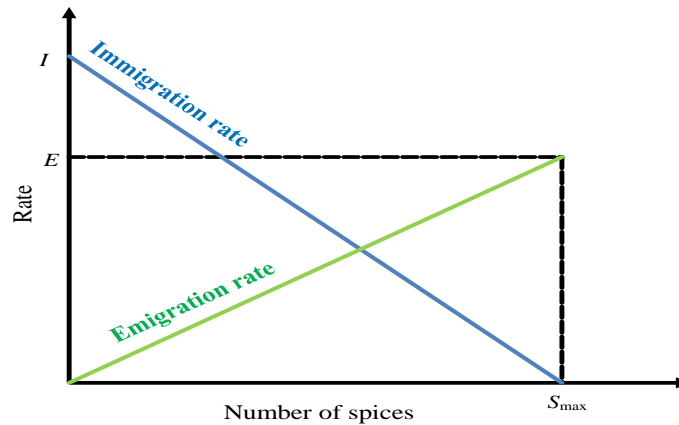


Figure 3. Migration rates vs. number of species

A variable called Habitat Suitability Index (HSI) is assigned for each habitat. More than the rate of immigration decreases and the rate of emigration increases more HSI of the habitat increases, and vice versa since the habitats with high HSI which are well suited to the residence of the species are more frequented. BBO is a population-based technique like GA. A detailed study in [20] for the similarities and dissimilarities between the characteristics of BBO and GA. In the BBO algorithm, individuals that are represented by chromosomes in GA, are represented by habitats. The fitness of each candidate habitat is its HSI. Habitats with high HSI correspond to the best solutions. Mutation and migration operators are the two main operators for BBO, as for GAs. Migration includes emigration and immigration.

#### A. Migration operators

To provide an improved solution to the optimization problem, immigration and emigration operators are used.

Let consider  $N = S_{max}$ . Equations (10) and (11) respectively express the immigration and emigration rates of  $k$

species in the habitat as shown in Figure 3.

$$\lambda_k = I \left( 1 - \frac{k}{N} \right) \quad (10)$$

$$\mu_k = \frac{Ek}{N} \quad (11)$$

Since each solution  $X = (x_1, x_2, \dots, x_n)$  is considered a habitat for this BBO algorithm and  $n$  is the number of decision variables. These variables are called Suitability Index variables (SIVs). By assigning each decision variable an SIV. A pre-specified probability  $P_{mod}$  is used to modify All

solutions. All SIVs of the solution to be modified will migrate according to the immigration rate of the corresponding habitat. This standardized immigration rate is given by Equation (12). Once SIV is selected to migrate, the emigration rate is used to determine which of the other solutions must migrate its SIV to the solution to be changed.

$$\lambda_k \leftarrow \lambda^l + \frac{(\lambda^u - \lambda^l)(\lambda_k - \lambda^{\min})}{(\lambda^{\max} - \lambda^{\min})} \quad (12)$$

Where,  $\lambda^{\min}$  and  $\lambda^{\max}$  are minimum and maximum bounds of the immigration rate, respectively.  $\lambda^l$  and  $\lambda^u$  are lower and upper limits of the normalized immigration rate, respectively.

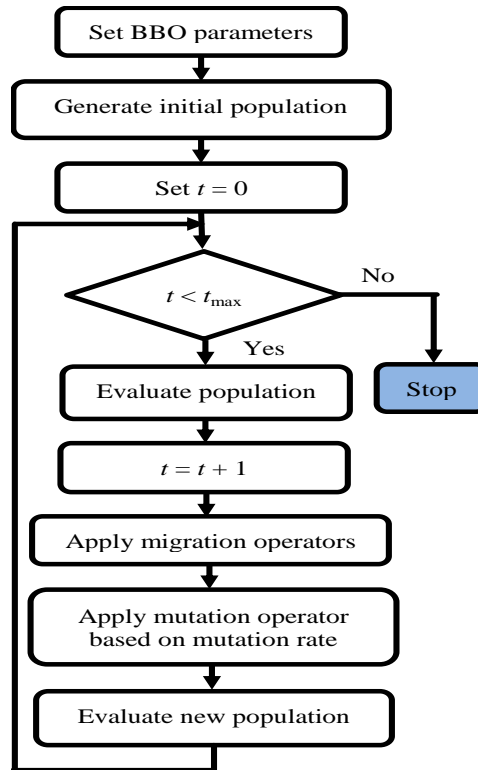


Figure 4. Flowchart of the proposed optimization algorithm

### B. Mutation operator

In the sudden immigration of a large number of species from a neighboring habitat, the HSI of each habitat can undergo drastic changes due to climate change, natural disasters, diseases. This random change is modeled by a mutation operator in the BBO algorithm. After application of the migration operators, the SVI of the number of habitats of the population obtained will be modified using a mutation operator according to the mutation rate [21]. This mutation is applied in order to obtain the diversity of the population at the next iteration, like in GA. Regarding the most BBO-based optimization techniques, the mutation rates for each H habitat depend on the probability that P of this habitat contains S species. As shown in reference [16],  $P_s$  is updated. for each time step  $\Delta t$  as follows.

$$P_s(t + \Delta t) = P_s(t)(1 - \lambda_s \Delta t - \mu_s \Delta t) + P_{s-1} \lambda_{s-1} \Delta t + P_{s+1} \mu_{s+1} \Delta t \quad (13)$$

For  $\Delta t \rightarrow 0$ , equation (13) can provide the following expression.

$$\dot{P}_s = \begin{cases} -(\lambda_s + \mu_s)P_s + \mu_{s+1}P_{s+1}; & S = 0 \\ -(\lambda_s + \mu_s)P_s + \lambda_{s-1}P_{s-1} + \mu_{s+1}P_{s+1}; & 1 \leq S \leq S_{\max} - 1 \\ -(\lambda_s + \mu_s)P_s + \lambda_{s-1}P_{s-1}; & S = S_{\max} \end{cases} \quad (14)$$

The mutation rate can be described as follows.

$$m_s = m_{\max} \left( 1 - \frac{P_s}{P_{\max}} \right) \quad (15)$$

Where  $m_{\max} \in [0,1]$  is a pre-specified parameter.  $P_{\max} = \max \{P_1, P_2, \dots, P_N\}$ .

In our study, the non-uniform mutation operator has been employed. So, at the  $t$ -th iteration, each SIV will be transformed to other SIV' with a probability as follows.

$$SIV' = \begin{cases} SIV + \Delta(t, b - SIV), & \text{if } \tau=0 \\ SIV - \Delta(t, SIV - a), & \text{if } \tau=1 \end{cases} \quad (16)$$

$$\Delta(t, y) = y \left( 1 - r \left( 1 - \frac{t}{t_{\max}} \right)^\beta \right) \quad (17)$$

Where  $\tau$  is a binary number,  $r$  is a random number and  $t_{\max}$  is the maximum number of iteration.  $a$  and  $b$  are lower and upper bounds of the corresponding SIV.  $\beta$  represents the dependency degree on the iteration number. The flowchart of the proposed BBO algorithm with mutation operator is given in Fig. 4.

#### IV. IMPLEMENTATION OF THE PROPOSED ALGORITHM

Having been applied for the first time to solve one of the main power system problems which is the EED problem, the BBO will be tested in this section on ten unit power system. In order to demonstrate the effectiveness of the proposed optimization technique, a comparison with BBO algorithm and more than ten metaheuristic-based techniques used for solving the power dispatch problem is presented. Results have been obtained using MATLAB R2009a installed on a PC with i7-4510U CPU @ 2.60 GHz, 64 bit.

##### A. EED problem for the ten-unit system without POZs

To further demonstrate the applicability of this method for real power network, a large test system is also used that is the forty-unit system with VPLE. The EED problem is performed for this system with total power demand  $P_D$  of 2000 MW. Fuel cost coefficients, emission coefficients and operating limits of generators are taken from [18]. For validation, the proposed algorithm has been compared with other techniques that are recently used in the literature to solve the EED problem for the ten-unit system. The fitness function given in equation (3) has been minimized for  $\lambda = 1.38501$  \$/ton. Convergence characteristics of fuel cost and emission functions using BBO algorithm are depicted in Fig. 5 and front Pareto Solutions in Fig.6.

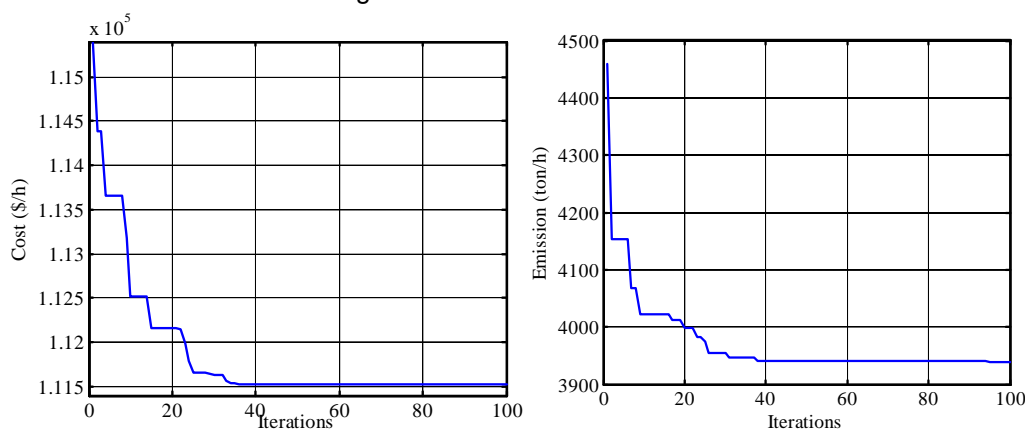


Figure 5. Convergence of the proposed algorithm of the Ten unit system without POZ

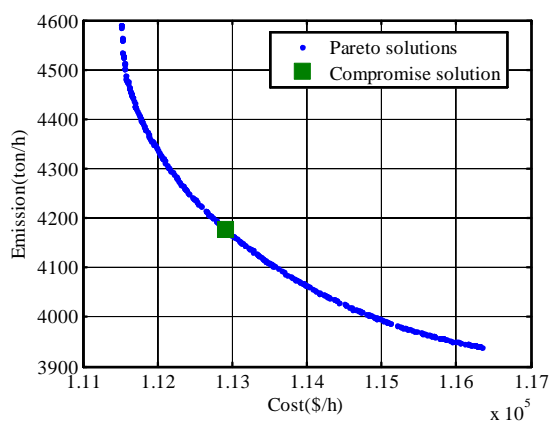


Figure 6. Pareto Solutions of the Ten unit system without POZ

Best solution for minimum cost, minimum emission and best compromise solution extracted from the Pareto front are tabulated in Table 1. Results for the proposed algorithm BBO and several techniques proposed in the literature [22-28] such as NSGAII and MOPSO-based methods, are compared in Table 2. It is clear that the proposed BBO provides the cheapest generation cost and the lowest emission that are around 112906 \$/h and 4176 ton/h as a compromise solution respectively.

**B. EED problem for the ten-unit system with POZs**

In this case, the ten-unit system is used to prove the feasibility of BBO for solving the EED problem including all operating constraints such as VPLE and POZ constraints. The problem becomes with high nonlinearity and more complicated. The B-loss matrix of the ten-unit system is given below.

$$B = 10^{-4} \begin{bmatrix} 0.49 & 0.14 & 0.15 & 0.15 & 0.16 & 0.17 & 0.17 & 0.18 & 0.19 & 0.20 \\ 0.14 & 0.45 & 0.16 & 0.16 & 0.17 & 0.15 & 0.15 & 0.16 & 0.18 & 0.18 \\ 0.15 & 0.16 & 0.39 & 0.10 & 0.12 & 0.12 & 0.14 & 0.14 & 0.16 & 0.16 \\ 0.15 & 0.16 & 0.10 & 0.40 & 0.14 & 0.10 & 0.11 & 0.12 & 0.14 & 0.15 \\ 0.16 & 0.17 & 0.12 & 0.14 & 0.35 & 0.11 & 0.13 & 0.13 & 0.15 & 0.16 \\ 0.17 & 0.15 & 0.12 & 0.10 & 0.11 & 0.36 & 0.12 & 0.12 & 0.14 & 0.15 \\ 0.17 & 0.15 & 0.14 & 0.11 & 0.13 & 0.12 & 0.38 & 0.16 & 0.16 & 0.18 \\ 0.18 & 0.16 & 0.14 & 0.12 & 0.13 & 0.12 & 0.16 & 0.40 & 0.15 & 0.16 \\ 0.19 & 0.18 & 0.16 & 0.14 & 0.15 & 0.14 & 0.16 & 0.15 & 0.42 & 0.19 \\ 0.20 & 0.18 & 0.16 & 0.15 & 0.16 & 0.15 & 0.18 & 0.16 & 0.19 & 0.44 \end{bmatrix} \quad (18)$$

Total cost and emission functions will be minimized individually and simultaneously according to the power demand PD in MW. Unit data are taken from [18]. Generation schedule in MW using BBO algorithm for front Pareto Solutions of fuel cost and emission function with POZ constraints is shown in Fig 7. In addition, it can be seen that when total cost in \$/h is minimized, the total emission in ton/h is at its maximum value and vice versa.

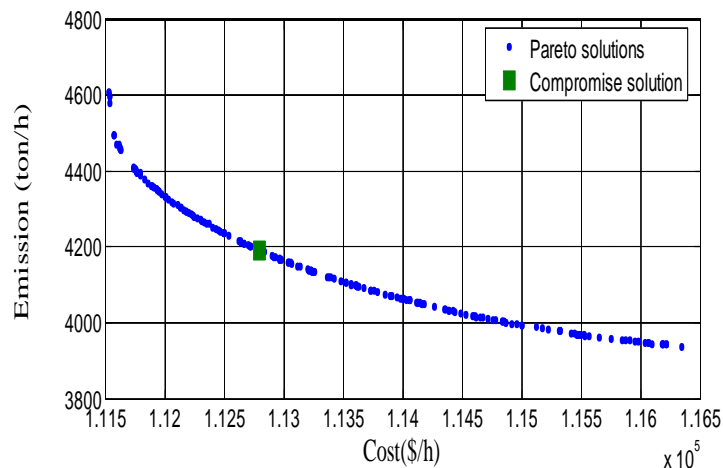


Figure 7. Pareto Solutions of the Ten unit system with POZ

TABLE 1. OPTIMUM GENERATION IN MW FOR PD = 10500 MW USING BBO ALGORITHM.

	Minimum cost	Minimum Emission	Compromise Solution
P1	54.3119	54.9189	54.9958
P2	79.6698	75.6915	79.6828
P3	116.0014	78.9341	88.1911
P4	100.1478	79.6363	85.0721
P5	83.6505	158.4241	128.3153
P6	76.2487	239.9714	148.1736
P7	299.7389	294.7465	297.4553
P8	339.0521	300.5536	321.0205
P9	468.500	397.6924	441.6506
P10	469.6871	401.2364	440.0315
Cost (\$/h)	111534	116348	112794
Emission (ton/h)	4608	3937	4190
Losses (MW)	87.0085	81.8051	84.5885

TABLE 2. COMPARISON WITH OTHER META-HEURISTIC TECHNIQUES (TEN-UNIT SYSTEM, 2000 MW).

	Minimum cost			Minimum Emission			Compromise Solution		
	With CBBO	With MOPSO	With NSGAI	With CBBO	With MOPSO	With NSGAI	With CBBO	With MOPSO	With NSGAI
P1	54.8956	54.9999	54.7824	54.8214	54.9455	54.9126	54.8799	54.9704	54.9875
P2	79.9981	74.1543	79.6555	73.0994	79.8454	75.8895	78.8306	78.7160	77.6534
P3	109.6777	99.3913	87.7777	87.2102	81.8472	76.0226	87.7033	86.8131	80.0651
P4	102.8462	103.4706	97.9282	81.5546	84.1212	81.4785	83.5823	85.0392	84.3108
P5	87.1997	92.6824	97.7244	160.0000	159.9553	160.0000	133.3311	133.0219	139.1104
P6	74.6702	89.0310	106.6724	238.7611	231.0996	238.0721	149.2570	152.7218	163.6017
P7	298.5086	299.8666	289.6461	292.5171	280.8557	273.3706	295.6187	297.7803	288.3222
P8	339.5090	334.2644	333.4564	294.3314	302.8003	314.0412	318.8995	319.2379	325.0241
P9	469.8485	469.9252	469.1623	397.3514	406.5345	415.6467	441.1648	437.2097	444.0404

P10	469.8811	468.9854	469.7723	402.0187	399.8273	392.4622	441.2869	438.8710	426.9918
Cost (\$/h)	111519	111590	111706	116347	116014	116282	112906	112985	113360
Emission (ton/h)	4590	4514	4432	3939	3946	3946	4176	4165	4129
Losses (MW)	87.0347	86.7711	86.5778	81.6653	81.8320	81.8962	84.5541	84.3814	84.1072

Shaded columns correspond to the results provided by the proposed algorithm.

## V. CONCLUSION

Economic emission dispatch (EED) is a difficult optimization problem in the operation of the electrical system. The quality of its optimal solution is influenced by the operating constraints, such as the prohibited operating zones and the load effects of the valve. In this context, this study presented an optimization based on Cauchy biogeography (BBO) to solve the EED problem. All the above constraints have been considered. In addition, the power balance constraint was considered. The validation of the proposed optimization algorithm has been verified on ten unit test system. The results of comparison with more than ten metaheuristic techniques used recently in the literature show that the proposed algorithm gives the best optimal solutions. Therefore, according to the results, BBO can be presented as an algorithm capable of EED problem.

## REFERENCES

- [1] C.L. Chen & C.L. Wang, Branch-and-bound scheduling for thermal generating units, *International Journal of Industrial Mathematics*, 4(3), 163-170, 2012.
- [2] A.J. Wood & B.F. Wollenberg, *Power Generation, Operation and Control*, 1994, Wiley, New York-USA.
- [3] C.W. Gar, J.G. Aganagic, B. Tony Meding Jose & S. Reeves, *Experience with mixed integer linear programming based approach on short term hydrothermal scheduling*, *IEEE Transaction on Power Systems*, 16(4), 743-749, 2001.
- [4] C.E. Lin, S.T. Chen & C.L. Huang, A direct Newton-Raphson economic dispatch, *IEEE Transactions on Power Systems*, 7(3), 1149-1154, 1992.
- [5] J.B. Park, K.S. Lee, J.R. Shin & K.Y. Lee, A particle swarm optimization for economic dispatch with nonsmooth cost functions, *IEEE Transaction on Power Systems*, 20, 34-42, 2005.
- [6] Liang Z, Glover JD. A zoom feature for a dynamic programming solution to economic dispatch including transmission losses. *IEEE Trans Power Syst* 1992;7:544-550.
- [7] Torres G, Quintana V. On a nonlinear multiple centrality corrections interior-point method for optimal power flow. *IEEE Trans Power Syst* 2001;16(2):222-228.
- [8] Ganjefar S, Tofighi M. Dynamic economic dispatch solution using an improved genetic algorithm with non-stationary penalty functions. *Eur Trans Electr Power* 2011;21(3):1480-1492.
- [9] Tlijani K, Guesmi T, Hadj Abdallah H. Extended dynamic economic environmental dispatch using multiObjective particle swarm optimization. *Int J Electr Eng Inf* 2016;8(1):117-131.
- [10] Panigrahi CK, Chattopadhyay PK, Chakrabarti RN, Basu M. Simulated annealing technique for dynamic economic dispatch. *Electr Power Compon Syst* 2006;34(5):577-586.
- [11] Ziane I, Benhamida F, Graa A. Simulated annealing algorithm for combined economic and emission power dispatch using max/max price penalty factor. *Neural Comput Applic* 2016:1-9. DOI 10.1007/s00521-016-2335-3.
- [12] Sen T, Mathur HD. A new approach to solve economic dispatch problem using a hybrid ACO-ABC-HS optimization algorithm. *Electr Power Energy Syst* 2016;78:735-744.
- [13] Lin WM, Cheng FS, Tsay MT. An improved Tabu search for economic dispatch with multiple minima. *IEEE Trans Power Syst* 2002;17(1):108-112.
- [14] Jiang X, Zhou J, Wangc H, Zhang Y. Dynamic environmental economic dispatch using multiobjective differential evolution algorithm with expanded double selection and adaptive random restart. *Electr Power Energy Syst* 2013;49: 399-407.
- [15] Vaisakh K, Praveena P, Naga Sujatha K. Solution of dynamic economic emission dispatch problem by hybrid bacterial foraging algorithm. *Int J Comput Sci Electron Eng* 2014;2(1):58-64.
- [16] Simon D (2008) Biogeography-based optimization. *IEEE Trans Evol Comput* 12:702-713.
- [17] Pandit N, Tripathi A, Tapaswi S, Pandit M. An improved bacterial foraging algorithm for combined static/dynamic. *Appl Soft Comput* 2012;12:3500-3513.
- [18] M. Basu. Economic environmental dispatch using multi-objective differential evolution. *Applied Soft Computing* 11 (2011) 2845-2853.
- [19] Ahrari A, Atai AA. Grenade explosion method-A novel tool for optimization of multimodal functions. *Appl Soft Comput* 2010;10:1132-1140.

- [20] Zhang GH, Gao L, Shi Y (2010) A novel variable neighborhood genetic algorithm for multi-objective flexible job-shop scheduling problems. *Adv Mater Res* 118–120:369–373
- [21] Zhang GH, Gao L, Shi Y (2011) An effective genetic algorithm for the flexible job-shop scheduling problem. *Experts System with Applications* 38(4):3563–3573
- [22] Labbi Y, Ben Attous D, Mahdad B. Artificial bee colony optimization for economic dispatch with valve point effect. *Front Energy* 2014;8(4):449-458.
- [23] Sinha N, Chakrabarti R, Chattopadhyay PK. Evolutionary programming techniques for economic load dispatch. *IEEE Trans Evol Comput* 2003;7(1):83-94.
- [24] Sharma R, Samantaray P, Mohanty DP, Rout PK. Environmental economic load dispatch using multi-objective differential evolution algorithm. *International Conference on Energy, Automation, and Signal (ICEAS), India, 28-30 december 2011.*
- [25] Amjady N, Nasiri-Rad H. Solution of nonconvex and nonsmooth economic dispatch by a new adaptive real coded genetic algorithm. *Expert Syst Appl* 2010;37(7):5239-5245.
- [26] Pothiya S, Ngamroo I, Kongprawechnon W. Ant colony optimization for economic dispatch problem with non-smooth cost functions. *Electr Power Energy Syst* 2010;32(5):478-487.
- [27] Yang XS, Hosseini SSS, Gandomi AH. Firefly algorithm for solving non-convex economic dispatch problems with valve loading effect. *Appl Soft Comput J* 2012;12(3):1180-1186.
- [28] Basu M. Dynamic economic emission dispatch using nondominated sorting genetic algorithm-II. *Electr Power Energy Syst* 2008;30:140-149.